Microclimatic and Topographic Controls of Fire Radiative Energy in Southeastern Ohio

A thesis presented to

the faculty of

the College of Arts and Sciences of Ohio University

In partial fulfillment

of the requirements for the degree

Master of Arts

Loredana G. Suciu

August 2009

This thesis titled

Microclimatic and Topographic Controls of Fire Radiative Energy in Southeastern Ohio

by

LOREDANA G. SUCIU

has been approved for

the Department of Geography

and the College of Arts and Sciences by

James M. Dyer

Associate Professor of Geography

Benjamin M. Ogles

Dean, College of Arts and Sciences

ABSTRACT

SUCIU, LOREDANA G., M.A., August 2009, Geography

Microclimatic and Topographic Controls of Fire Radiative Energy in Southeastern Ohio

(82 pp.)

Director of Thesis: James M. Dyer

This study explores the environmental control of two key elements of water balance on fire behavior at two sites in southeastern Ohio, Arch Rock and Tar Hollow. The two elements of water balance are potential evapotranspiration (PET) and actual evapotranspiration (AET). Fire behavior is expressed in this study as fire radiative energy (FRE), which is estimated from time-sequence fire radiative power by remote sensing of infrared radiation during fires. Previous studies have shown that both fuel moisture and fuel load are primary driving forces of fire behavior at a coarse scale. Therefore, in this study, PET is used to suggest fuel moisture in spring and AET is used as a surrogate for productivity during the growing season in order to explain FRE at a fine scale. Results show that a water balance approach helped to explain FRE using categorical AET and PET. At the pixel level, the water balance approach was less successful because the variables did not relate reasonably with space and because of other fine-scale local effects (hydrology, decomposition rates) that were not captured by PET and AET. Aspect strongly influences solar radiation and PET. Thus, aspect was used additionally to assess its indirect effects on FRE. Overall, FRE responded well to aspect at both study sites.

Approved: _____

James M. Dyer

Associate Professor of Geography

ACKNOWLEDGMENTS

I express my gratitude to my advisor James Dyer (Department of Geography, Ohio University) for continuous mentoring and support in pursuing the goals of this study. This research would not be possible without the support from Matthew Dickinson (USDA Forest Services) and Valerie Young (Department of Chemical and Biomolecular Engineering, Ohio University) who financed and guided the work with fire images in a bigger framework of which this study had a small contribution. I would like to acknowledge Robert Kremens and Eugenie Song (College of Imaging Science, Rochester Institute of Technology, New York) for the two fire data sets used in this study. I also thank Anthony Bova (USDA Forest Services) for his constructive criticism to my first attempts in deriving significant relationships.

TABLE OF CONTENTS

Page

LIST OF TABLES

Page

LIST OF FIGURES

Page

INTRODUCTION

Prescribed-fires, controlled combustions of forest fuels, have been used to sustain oak regeneration in eastern deciduous forests. Studies about productivity of a site and fuel moisture are very useful for prescribed-burn practices because both are direct drivers of fire behavior. Knowledge of fuel availability, fuel continuity and fuel moisture helps in setting up ignition strategies, designing fuel measurements needed for fire spread models and estimates of fire intensity, and understanding fire limitations across the landscape. Optimizing ignition locations based on information about spatially-distributed fuel moisture and availability can maximize the efficiency of prescribed burning in a forest by avoiding incomplete combustion of wet and large fuels and, consequently, air pollution. Carbon monoxide (CO) is a common product of incomplete combustion affecting endangered species in southeast Ohio, such as Indiana bats (*Myotis sodalis*).

Productivity can be estimated from photosynthetic resources, such as energy and water. In this context, actual evapotranspiration (AET) becomes a predictor of net primary productivity during the growing season because it provides a simultaneous measure of water and energy availability in an environment (Rosenzweig 1968). In turn, productivity can inform fuel load as a measure of increase in biomass. Potential evapotranspiration (PET), a measure of water demand, linearly relates to temperature and radiation load, and therefore can be used to predict fuel moisture.

This thesis contributes to a joint project between USDA Forest Services and Ohio University, which uses aerial infrared imagery from fire to estimate fire energy release and fuel consumption, in order to simulate smoke transport and to assess toxicological

effects of CO on *Myotis sodalis*. Specifically, this thesis assists the estimation of fire radiative energy (FRE) or total heat release for two study areas in southeastern Ohio.

FRE represents the time-integrated heat flux estimated from fire radiative power (FRP) measured in infrared. Coarse-scale FRE (satellite-retrieved) was used previously to estimate fuel consumption and atmospheric pollution (Wooster et al. 2005), but no fine-scale FRE (airplane-retrieved) was used yet to inform about fire behavior and about the extent of which the environment controls FRE. Furthermore, climatic and physical drivers of burned area were previously analyzed at a continental scale (Archibald et al. 2009), but no study has used water budget elements as direct fire energy drivers at a landscape scale. Therefore, the theme of this study is to relate energy released from two fine-scale fires with water budget variables through estimates of productivity and fuel moisture. This study has two main goals:

1. Estimate fire energy release from two prescribed-fires

The estimation of FRE is based on the experimental knowledge that a fire front shows a peak in FRP close to the interface between fire front and the unburned fuel. Therefore, by extracting firelines from infrared images the peak in FRP can be identified with respect to distance from firelines. Then the peak can be used to estimate FRE assuming that after reaching the peak, radiative power cools down exponentially with time (Young VL, personal communication 2009). Thus, the objectives for estimating heat release include:

- To model firelines from time-sequence infrared imagery
- To extract peak FRP
- To integrate the peak FRP over time and estimate FRE

- To classify and map FRE

2. Assess microclimatic and topographic effects on FRE

A second goal focuses on fine-scale climatic and topographic drivers of FRE. Two hypotheses with objectives are described as follows:

Hypothesis 1: Growing season AET, due to its influence on productivity, can inform about fuel availability and therefore predict FRE. Theoretically, more productive sites will have greater biomass (fuel) and should release more heat. AET was previously used to predict site productivity (Rosenzweig 1968). Two objectives are designed for this hypothesis:

- To estimate growing season AET and to correlate with measured litter load
- To correlate AET with FRE
- To correlate FRE with measured litter load

Hypothesis 2: Spring PET can be used as a surrogate for fuel moisture to predict FRE since it incorporates temperature and solar radiation. Dry sites burn quicker and release high heat over short time; wet sites burn slower and release low heat over long time. Specific objectives are:

- To compute spring season PET
- To correlate spring PET with FRE
- To explore the indirect effect of topography by aspect on FRE

Topography controls the availability of both water and energy and fire behavior. For instance, aspect strongly influences the amount of solar radiation (Bennie et al. 2008), while solar radiation drives potential evapotranspiration (Turc 1961). Therefore, it is expected that, indirectly, aspect would factor in the FRE pattern during spring.

LITERATURE REVIEW

Fire Radiative Energy

A fire spreads primarily by virtue of heat transfer and flaming combustion (Johnson and Miyanishi 2001). Fire intensity is the product between heat of combustion (J/kg), mass of fuel consumed by the flaming front (metric tons/ha), and rate of spread (m/min). Fireline intensity is intensity per length of fire front expressed in kW/m, also known as the Byram index (Byram 1959).

An analogous to the *in situ* measured fire intensity is the remotely-sensed thermal response from fire. The thermal response can be separated theoretically into two components, one derived from the other: the instantaneous heat flux or *Fire Radiative Power* (FRP, kW/m^2) and the time-integrated heat flux also called *Fire Radiative Energy* (FRE, kJ/m^2). The former is particularly important for smoke transport simulations; the latter is central for determining fuel consumption and predicting ecological effects. The concept of *in situ* measured FRE was previously used in detecting thermal signal associated with fire (Hirsch et al. 1971, Waggoner 1991, Kaufman et al. 1996). Kaufman et al. (1996) introduced the concept of *remotely-sensed* FRE and directly related the thermal response to fire intensity and rate of vegetation burned. The concept was initially applied to wildfires using Moderate Resolution Imaging Spectroradiometer - MODIS (Kaufman and Justice 1998, Kaufman et al. 1998).

The great majority of remote sensing studies have been concerned with *spaceborne* heat flux from natural fires (Dozier 1981, Robinson 1991, Scholes et al. 1996, Prins and Menzel 1998, Giglio 2001, Justice et al. 2002, Wooster 2002, Wooster et al. 2003, Riggan et al. 2004, Smith and Wooster 2005, Wooster et al. 2005, Ichoku et al.

2008, Roberts et al. 2008) and only a few studies had concerned with *airborne* heat flux from controlled burns (Trollope et al. 1996, Oertel et al. 2003). Field studies in experimental burns and laboratory studies were conducted to test the relationships between heat flux, fuel consumption, and air emissions (Wooster 2002, Wooster et al. 2005, Freeborn et al. 2008).

The theory behind the FRE estimation is based on the physical process of biomass combustion. Traditionally, biomass consumption was assessed using theoretical equations and historical records of fire frequency or maps of burn scars. Given the difficulty of measuring on-the-ground fire parameters (i.e., area burned, fuel consumption), this method became more limited with the advent of satellite fire imagery. Wooster's (2003, 2005) alternative method is based on FRE derivation from pixel radiance (FRP) measured by spaceborne infrared sensors. Time integrated FRP in a pixel represents total FRE. In general, the pixel radiance method underestimates FRE derived from low resolution spaceborne FRP (Wooster et al. 2005). Therefore, it might be reasonable to expect more accurate FRE estimations and fuel consumption rates from airborne FRP (1m resolution) compared to spaceborne FRP (e.g., 370m to 4km resolution). This assumption involves accurate image airborne calibrations and image analysis. However, through image analysis (Wooster et al. 2005) and in theory as well (Wien's displacement law, Campbell 1996) it was determined that radiance in the long infrared wavelength saturates at a lower temperature than radiance in the mid-infrared. Therefore, a long infrared sensor may not detect the emitted radiance at much higher temperatures than its detection limit; pixels get saturated. The issue of saturated pixels must be carefully addressed for more accurate determination of total heat release.

One application of FRE is to map the total fuel consumed by fire. Wooster et al. (2005) derived an empirical equation linearly relating total fuel consumption (TFC) with fire radiative energy. This equation links the effect of burning near-surface to remotely-sensed FRE. In other words, more total fuel consumed means more total heat released from a pixel. In this context TFC can inform about one important aspect of fire behavior. Related to this, AET during growing season can inform about the physical and microclimatic template influencing that fire behavior in terms of fuel loading.

Physical and Climatic Drivers of Fire

Several authors have studied physical and climatic drivers of wildfire focusing on fuel load and moisture as drivers of fire intensity and fuel continuity as a driver of fire spread. Fire intensity and fire spread are two main factors affecting burned area. Archibald et al. (2009) used indirect drivers of fire to estimate fuel moisture (relative humidity and length of the dry season), fuel load (tree cover, rainfall, soil fertility and grazing) and fuel continuity (topography, land use and road density). They found that spatial variations in fuel moisture and fuel load are controlling fire at the continental scale.

Nepstad et al. (2004) analyzed spatial and temporal drought patterns in tropical forests to predict fuel flammability. Severe dry events can strongly impact fire, net primary productivity and carbon storage. During these events, soil water is depleted by potential evapotranspiration. Water loss below 25% of the available water capacity was found to be responsible for 25% reduction in leaf area index in Amazon forests, for example.

Girardin and Wotton (2009) also used drought index to assess summer wildfire risk across Canada. They found that 63% of the variation in annual burned area was explained by moisture availability in summer.

Overall, these studies support the theory that the primary driving forces of fire behavior are fuel moisture, fuel load and fuel continuity and that secondary factors, such as climate, soil fertility, topography and land use are controlling these forces. In addition, they point out that the wildfire risk increases with drought in semiarid environments, fire can impact the hydrology and vegetation, and that an additional heating of the atmosphere immediately after fire can affect the climate and, in turn, the fire regime at a coarse scale. Although none of these studies addresses hypotheses of fine-scale climatic and topographic influences of energy released from the fire, they can be useful to understand what controls productivity and flammability of a site, in particular in frequently burned areas.

Water Balance

A water balance approach provides a biologically meaningful indicator of moisture use and stress in an ecosystem (Dyer 2009). This water balance model is dynamic because it incorporates not only topographic but also climatic changes, providing absolute measurements of moisture use and stress in millimeters of water. This property confers to the model the quality of being easily adaptable for changes in climatic conditions. Static models, such as integrated moisture index (Iverson et al. 1997) do not provide measures of moisture in absolute terms but rather assign sites a value (e.g., 0-100%) derived from surface properties (hillshade, curvature, flow accumulation) and soil properties (available water holding capacity). Yang et al. (2009) also used an index, which measures the

catchment's landscape characteristics from three parameters: the relative infiltration capacity of the catchment, vegetation coverage and the average slope of the catchment.

Key element of the water balance include actual evapotranspiration (AET), which represents the actual water loss by plants, and potential evapotranspiration (PET) representing water demand by vegetation if water is not limiting. When PET exceeds AET (when water is a limiting factor in an environment), a deficit exists according to Equation 1. In temperate humid climates such as the eastern U.S., this condition is most likely to occur during summer.

$$PET = AET + Deficit \qquad (1)$$

On an annual basis, when precipitation (P) exceeds AET, a surplus of water becomes available in the environment (i.e., runoff) as can be inferred from Equation 2.

$$P = AET + Surplus \qquad (2)$$

Deficit is accompanied by an energy release in the form of sensible heat. This additional energy contributes to an increase in ground heat flux enhancing dryness in the absence of water supply (Zhang et al. 2004, Wendt et al. 2007) and together with wind can favor fire spread. However, note that wind convection is negligible near-surface, but becomes important at the vegetation-atmosphere interface (Campbell 1977, Bennie et al. 2008).

Many studies focused on estimating long-term actual evapotranspiration following Budyko's postulate, which describes the character of annual water balance as a function of precipitation (Zhang et al. 2004, Porporato et al. 2004, Potter et al. 2005, Gerrits et al. 2009). Budyko (1974) conceived a diagram of the evaporative index

(AET/P) and the dryness index (PET/P) as shown in Figure 1. According to this diagram, environments can be classified in arid or water limited (AET/P = 1 for PET/P >1) and humid or energy limited (AET/P = PET/P for PET/P <1).

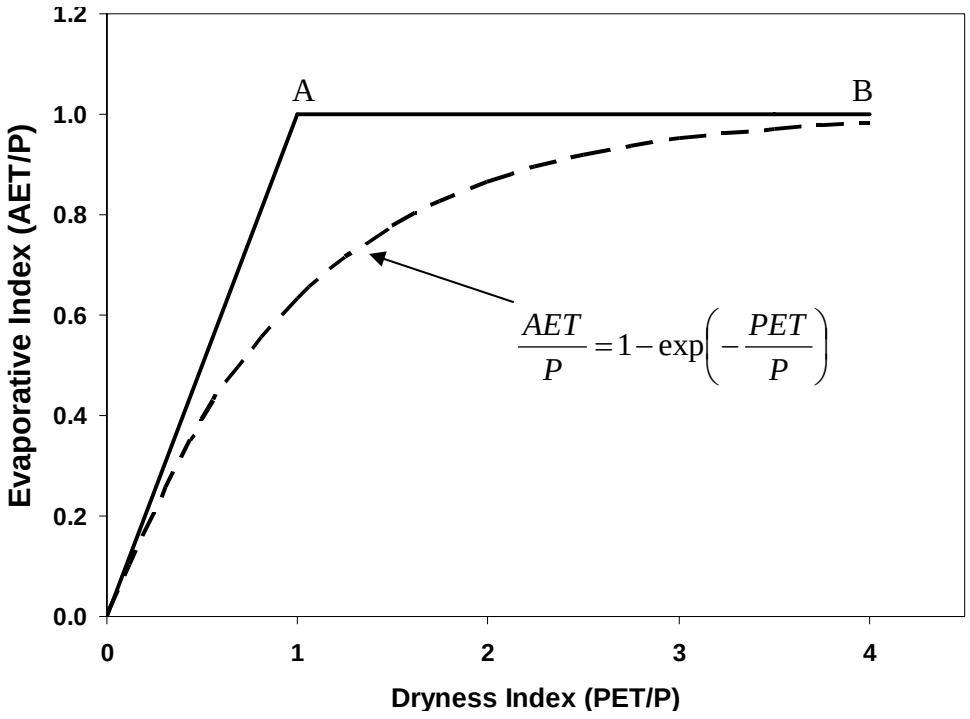

Figure 1. Budyko's curve (adapted from Budyko 1974).
Line *OA* is the energy-limit to evapotranspiration and *AB* the water limit. The dashed curve represents the relationship between the evaporative index and the dryness index.

Overall, these studies offer details about what is considered physically realistic in terms of evapotranspiration with respect to energy and hydrology at large spatial and temporal scales. However, according to Yang et al. (2009) these studies do not include fine spatial- and temporal-scale vegetation dynamics in their models. By plotting vegetation response on the Budyko curve, it was found that evaporation efficiency was sensitive to vegetation. Another limitation of these studies is that they do not consider the topographical effects on evapotranspiration.

Few studies modeled topographical effects on water balance and climate. McVicar et al. (2007) computed high resolution regional PET surfaces considering the topographical control on meteorological driving forces (temperature, wind speed, and vapor pressure). Dyer (2009) modeled PET grids at very fine spatial scales in southeastern Ohio and North Carolina taking into account topographical control on both energy and meteorological driving forces (solar radiation and temperature).

Slope and aspect control the amount of solar radiation intercepted by the surface, and solar radiation affects PET, near-surface microclimate and soil moisture (Bennie et al. 2008). Spatially explicit models (Bennie 2008, Dyer 2009) use digital elevation models to compute solar radiation for each grid cell. These models eliminate the problems of slope and aspect parameterization on which spatially implicit models are based. Spatially explicit models reproduce well the topographic variation of microclimatic conditions of a site using easily available data.

In brief, PET plays an important role in the energy-water balance model and many studies seek to understand the physical process of evapotranspiration at coarse spatial- and temporal-scales. In contrast, other studies are concerned with topographical variation in microclimate, which controls PET (i.e., spatially explicit models). The two categories of studies are useful to understand the process of evapotranspiration at coarse scales and to apply theoretical knowledge to model PET at fine scales within different environments. In the short term, soil moisture dynamics controls evapotranspiration; storage and rainfall are less important but they become important on annual time-scale because of their seasonality (Zhang et al. 2004).

METHODS

Study Areas

Two study areas were located in southeastern Ohio (Figure 2); Arch Rock is part of the Raccoon Ecological Management Area (Vinton County) and Tar Hollow is within Tar Hollow State Forest (Ross County). Both study sites lay within the mesophytic region of the eastern deciduous forests, belonging to the Low Hills Belt of the Unglaciated Allegheny Plateau (Braun 1950). Elevation is about 200-300 m above sea level; the topography is highly dissected (ca. 100 m total relief) determining strong microclimatic gradients, such as xeric west- and south-facing slopes vs. mesic north- and east-facing slopes (Albrecht and McCarthy 2006). Sedimentary bedrock and a temperate-continental climate characterize both study sites. The average annual temperature is 11.3 ºC and annual precipitation 1024 mm (NOAA 2004).

Prescribed-fires were conducted by USDA Forest Service at each site. The prescribed-burns were intended to alter the stand structure by killing thinner barked trees and encouraging seedbeds to support oak regeneration. The Arch Rock fire (17 April, 2004) burned in an area that was cleared for charcoal production in the mid- and late 1800's. Fire occurred frequently in this area until suppression in 1923 (Hutchinson et al. 2005). Prescribed-burning at this site began in 1995 and has continued since (Hutchinson et al. 2005). The Tar Hollow fire (20 April, 2007) burned in an area which experienced subsistence farming in the past, and which was almost completely harvested in the mid- and late 1800's. According to ODNR's Burn Plan, there is no documentation of fires since suppression began in 1920.

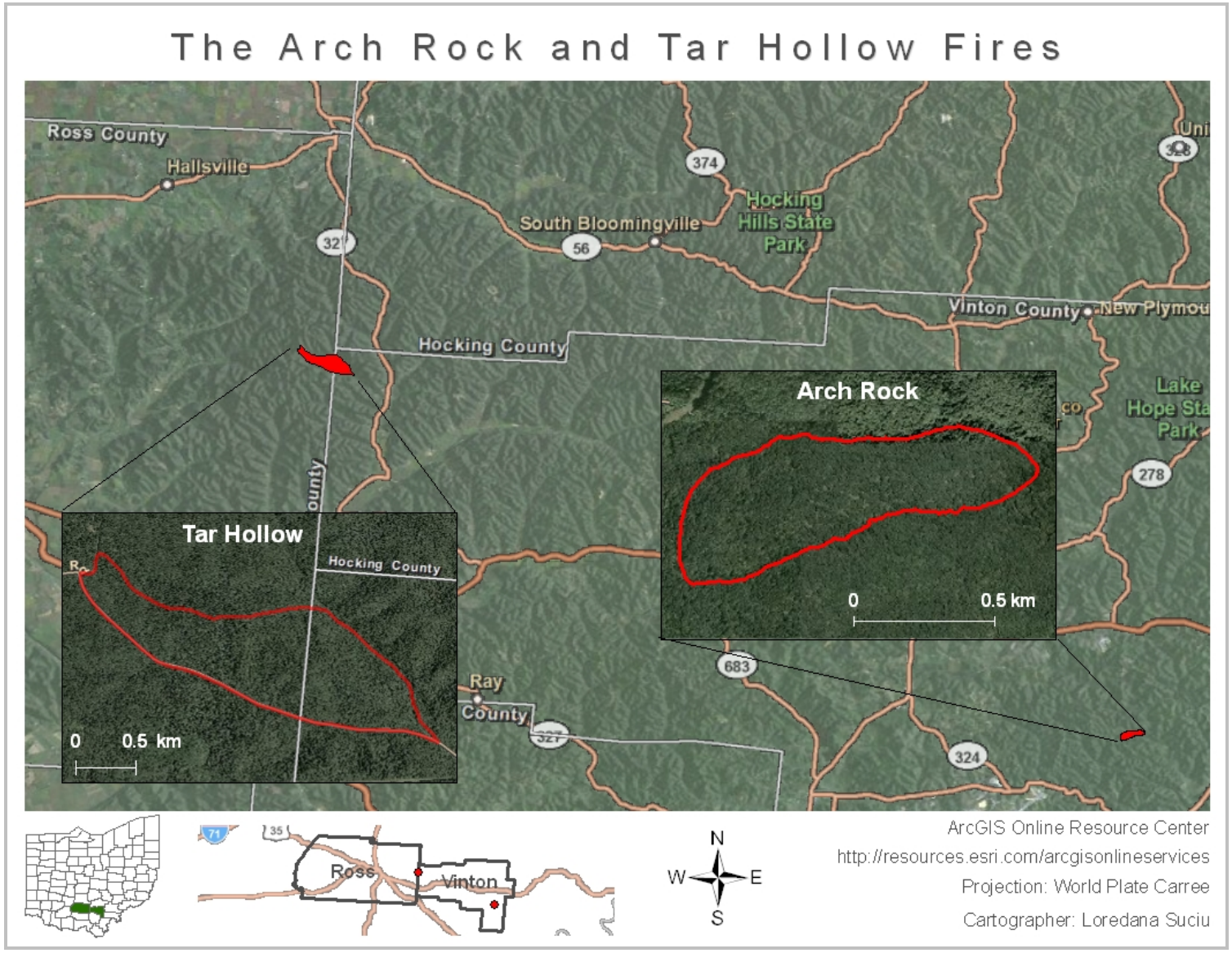

Figure 2. Study areas

Arch Rock has an east-west oriented ridge, and covers an area less than 0.25 km^2. The second-growth forest is dominated by mixed oak and hickory. In this unit, fire was conducted to burn at high intensity in particular on the upper portions of the south-facing slope and ridgeline. Ignition was started by five people with drip torches walking east-to-west, two people at the bottom of the slope, two at the mid-slope and one along the ridge. The fire was allowed to spread throughout the unit about two hours. Burn conditions were not optimal, with high humidity and recent rains; occasionally re-ignitions were necessary. The fuel that burned was mostly litter and twigs; no crown combustion occurred. The fire was monitored at the ground using thermocouples and IR sensors and remotely via airplane using an infrared detection system from Rochester Institute of Technology (NY).

Tar Hollow is three times larger than Arch Rock and is oriented northeast-southwest. Coves in the southwest part of the site provide different microclimate that can act as fire breaks. The stand composition is diverse with both shade intolerant and intermediate species, such as yellow poplar, red maple, cherry, oaks, sugar maple and locust. The understory on xeric sites consists of red maples while on mesic sites of sugar maples. Both terrestrial and aerial ignitions were used in this fire. Terrestrial point ignitions by drip torch were applied downwind from the ridge to create ignition lines with a width of at least 50 feet. The interior of the fire unit was ignited by a helicopter dispersing thousands of well-distributed ping-pong balls containing potassium permanganate, injected with ethylene glycol just before they were dropped into the unit. The relative distance between the ignition balls was 25 feet, while location from ignition lines at the ground was 100-200 feet (Mike Bowden, personal communication 2009).

This additional aerial ignition encouraged the progression of the lines ignited from the ground. Because Tar Hollow has no history of fire, the high fuel load available drove the fire to burn at higher intensity than at Arch Rock. Since the airborne long infrared sensor used at Tar Hollow had a lower dynamic range than the one used at Arch Rock, this resulted in saturation of the sensor. Moreover, the fire at Tar Hollow was encouraged by more conducive weather. Low relative humidity and no recent rain resulted in dry litter and larger fuels; some woody combustion occurred.

Data Needs and Sources of Data

Fire Images

The procedure of time-sequence airborne imaging consisted of multiple over-flights with a repeat interval of 3-6 minutes or less. Eleven time-sequence infrared images were taken at Arch Rock and twenty-nine at Tar Hollow. Images were acquired, registered and orthorectified by Rochester Institute of Technology and provided at 1 m resolution (Arch Rock) and 3 m resolution (Tar Hollow). A Dexter Research 2M Thermopile device was used to measure the surface temperature and the heat flux from a black body (Robert Kremens, personal communication 2008). The incident heat flux was estimated using Stefan-Boltzman law (Campbell 1996) and then compared with the measured heat flux from a black body using linear regression. The resulted calibration factor was 0.58 $W/counts/m^2$. After image calibration, each pixel measured fire radiative power (FRP) in W/m^2. The calibration for Tar Hollow imagery is still in progress due to sensor saturation problems. Calibration was possible for Arch Rock only because a better detection system was used (WASP-Wildfire Airborne Sensor Program) with a dynamic range in the long infrared channel of 0-16,000 counts (14 bits). For Tar Hollow, the detection system used

(WASP Lite) did not reproduce well the intensity in thermal signal expected from such a big fire because the sensor was easily saturated. The dynamic range in this case was 0-5,000 counts (12 bits). The estimated saturation plateau was around 3,600 counts and the background threshold about 2,000 counts; therefore, the variability in FRP for Tar Hollow was less than a factor of 2. For Arch Rock, variability in FRP was a factor of 5 considering the same background threshold (2,000 counts) and the saturation limit around 11,000 counts (90% of the maximum value).

Elevation

Digital Elevation Models (DEMs) in the form of ESRI ArcInfo Grids were downloaded from the Ohio Geographically Referenced Information Program (2008) web site. Elevation data had been already projected using the coordinate system NAD 1983 HARN State Plane Ohio South FIPS 3402 US Foot. Cell size is 2.5 feet (0.7 m). The vertical accuracy reported by OGRIP in the metadata file is ± 1 foot (RMSE = 0.5 foot at 95% confidence level). Elevation grids for both study sites were resampled to 9.8 feet (3 m) resolution for this study. The DEMs were used to compute solar radiation for each grid cell in order to estimate PET and to generate slope and aspect grids.

Solar Radiation

Hourly solar radiation (W/m^2) from 2003, 2004, 2006 and 2007 measured by Scalia Laboratory (2008) was used to parameterize solar radiation estimates at the study sites using the Solar Radiation toolset in ArcGIS 9.3, as described below.

Climate

Monthly temperature grids were needed for determination of PET, and precipitation grids were used in the computation of AET (see below). Therefore, minimum and maximum

monthly temperatures and precipitation grids at 800 m resolution were downloaded from the PRISM Climate Group (2008). Average monthly temperature and precipitation grids were computed for both study sites, at 1 m resolution for Arch Rock and 3 m resolution for Tar Hollow.

Available Water Capacity

Soil water-holding capacity, 0-100 cm depth, was obtained from digitized soil surveys from the Natural Resources Conservation Service (2008). Both spatial and tabular AWC were joined into a final shapefile that was converted to raster with units in mm.

Fuel measurements

About 40 fuel samples were taken at Arch Rock and 100 at Tar Hollow prior to fires. Hardwood leaf litter and herbaceous fuel were sampled within 3 m^2 plots at Arch Rock. At Tar Hollow only leaf litter, both upper (not decomposed) and lower (fermented), were sampled within 0.25 m^2 plots. Results were reported in kg/m^2 (Matthew Dickinson, personal communication 2009). Geographic projection of point location was WGS 1984 UTM Zone 17.

Extractions of Firelines and Peak FRP

Two preliminary steps for estimating energy released are the extraction of firelines and peak FRP. To identify peak FRP in each image it was necessary first to extract the active fire fronts (firelines) based on the knowledge that the hottest pixels are most likely to occur somewhere close to but behind the firelines. From the fire behavior point of view, the hottest locations may correspond to two different cases: backing (fires that burn against the wind) and heading (fires that spread with the help of wind). In a backing fire the heat transfer is mainly by radiation, while in a heading fire heat transfer is by both

convection and radiation. Consequently, backing fires release low heat compared to heading fires. Discrimination between backing and heading is important because they both have maxima in radiative power, but they may differ according to the type of combustion (smoldering vs. flaming). By using the firelines it was expected to account for this difference.

Fire images were analyzed in two environments: Remote Sensing (ENVI 4.5) and Geographical Information Systems (ArcGIS 9.3). The technique of image segmentation (Ononye et al. 2007, Parker 1997) was used to extract firelines. From each image, relevant features such as edges or rapid radiance changes were emphasized through cubic convolution and morphology. Cubic convolution facilitated edge detection (Laplacian filter) and radiance contrast (Sobel filter). Morphology (Dilation) changed the pixel size and type from row signal to byte signal (0-255). Boolean logic helped to select matching pixels from two inputs. For example, a Boolean AND condition selected identical locations of pixels with value 255 from two co-registered maps. Cubic B-spline approximated the firelines and accounted for geometrical shifts. The fireline algorithm is presented in Figure 3.

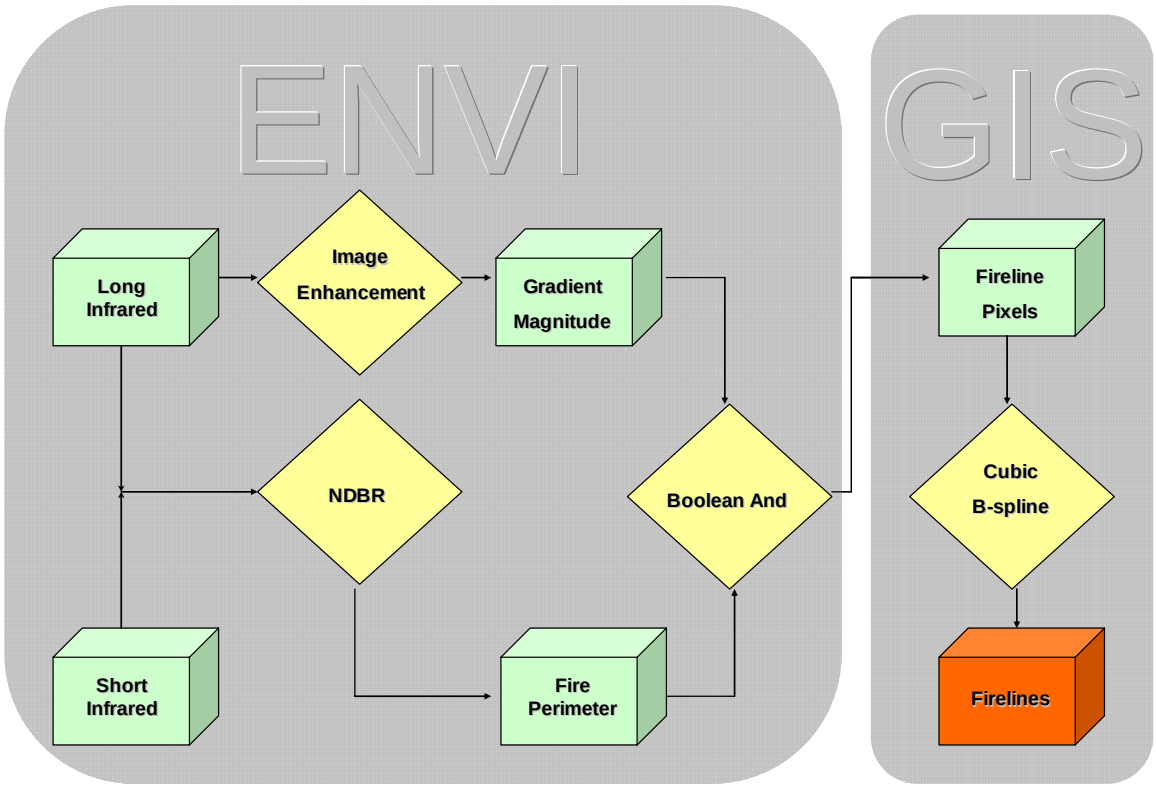

Figure 3. The algorithm used to extract firelines (adapted from Ononye et al. 2007).

Initially, burned area was extracted with the Normalized Difference Burned Ratio index (NDBR) for each IR image using Equation 3 (Ononye et al. 2007):

$$NDBR = \frac{SWIR - LWIR}{SWIR + LWIR} \qquad (3)$$

where SWIR is the Shortwave Infrared and LWIR is the Longwave Infrared. This NDBR ranging from -1 to 1 is a modification of the well-known NDVI (Normalized Difference Vegetation Index). Figure 4 provides an example of applied NDBR to extract burned area and fire perimeter. Figure 4a shows burned areas in black (negative NDBR) and unburned areas in white (positive NDBR) extracted from the third frame of the Arch

Rock dataset. NDBR was further subject to a Laplacian filter in order to extract the fire perimeter in Figure 4b and then treated by dilation for better approximation. In parallel, each image was convoluted with Sobel filter, enhancing the radiometric contrast and computing the gradient magnitude (GM) shown in Figure 5a-b. GM supported the validation of NDBR using the Boolean And logical operator. For instance, both GM and NDBR have the same scale 0-255. Pixels that are 255 in both images (GM and NDBR) are selected as fireline pixels.

The final output of image segmentation technique is a piecewise image that shows only the pixels defining the firelines. To favor the work in a vector environment, lines were edited through some of the selected pixels and cubic B-spline was used to approximate the firelines. In principal, cubic B-spline is an approximation tool that fits curves to relevant points. The input for this approximation in a GIS environment requires a continuous angled line edited through at least 9 pixels. This operation was done for each image-related fire line pixels in GIS, prior using the cubic approximation.

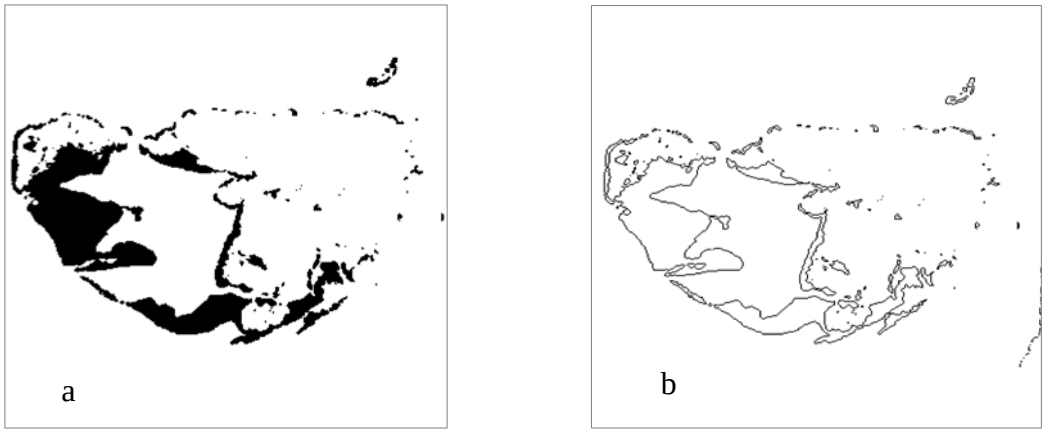

Figure 4. a) NDBR and b) fire perimeter.

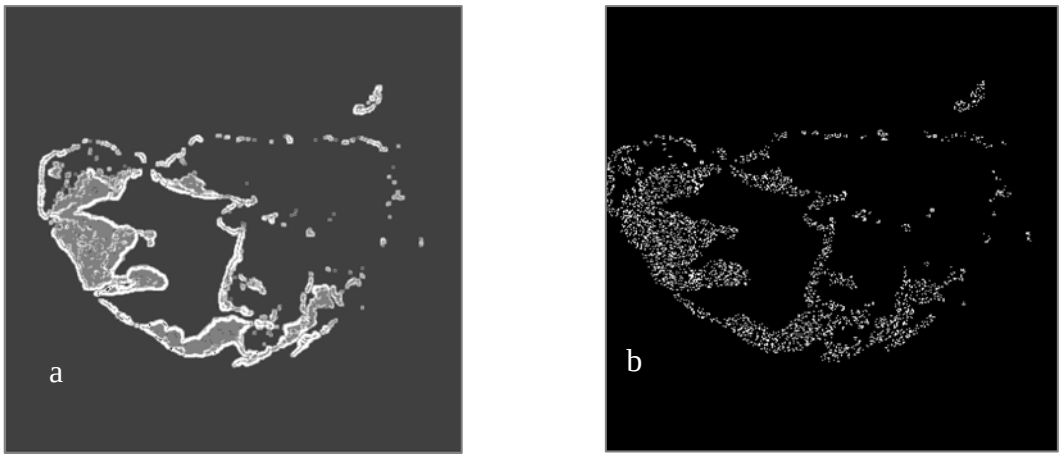

Figure 5. a) GM image and high b) GM pixels only.

After smoothing the angled lines (now the firelines should reproduce the elliptical shape of real active fire fronts), each image was analyzed individually in ArcGIS 9.3 to observe where the peak FRP was most likely to be with respect to firelines by overlapping Euclidean distance grids. An example of peak FRP extraction from a single image is presented in Figure 6. A peak was considered to be the hottest pixel immediately behind the fireline. Its neighbors must be colder for the pixel to be considered a peak. It was important to know the direction of the fireline. Direction was known by observing propagation of the fireline through 2-3 subsequent images. It could also be computed with the Euclidean distance tool. Each distance grid was built from a particular line feature and overlaid with the IR image and the fireline extracted from that image. Whenever peaks were sighted, the distance between peak and the fireline was measured. Then, distance grids were reclassified in two classes (0 and 1), so that 1 indicated the expected distance of the peak from fireline. This operation was repeated for each fireline in an image. Notice that each image contained several firelines.

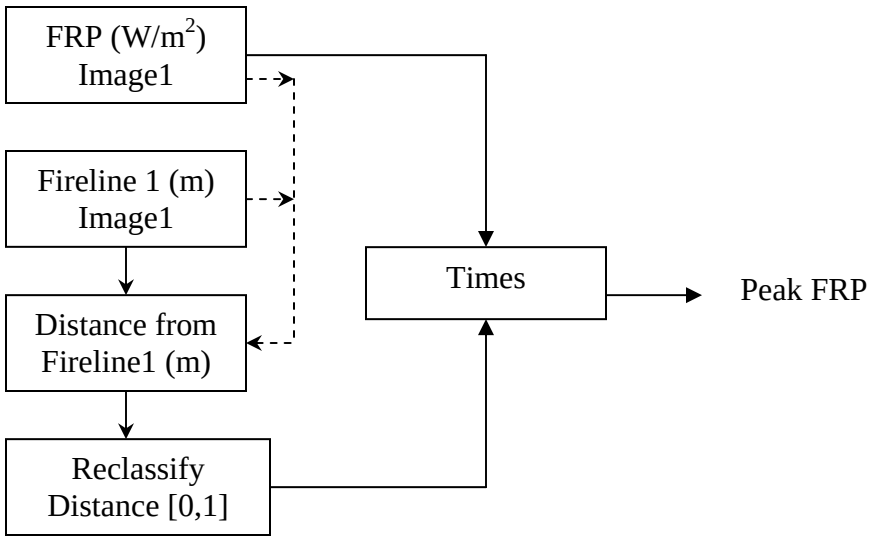

Figure 6. The diagram of peak FRP extraction

The peak digital count (peak DC) at Tar Hollow is analogous to peak FRP at Arch Rock. The only difference is that peak DC is not calibrated and, therefore, it cannot be named peak FRP. However, in terms of patterns, the two measures are comparable, since FRP is related to peak digital count by a constant. Since the goal of this study is to assess geographically the relative importance of microclimate and topography in fire behavior, it was necessary to use peak DC to estimate heat released. Saturation was also taken into account by applying a 90% limit to the presumed peak DC as estimated through the analysis of each image's histogram. In contrast to Arch Rock, the identification of peak DC was done by observing the peak above the mean and below the saturation limit. Histograms and saturation limits were computed for 29 images. An example of peak selection using image histogram is provided in Figure 7. Here, the peak can be anywhere within the interval defined by the peak DC threshold and saturated DC.

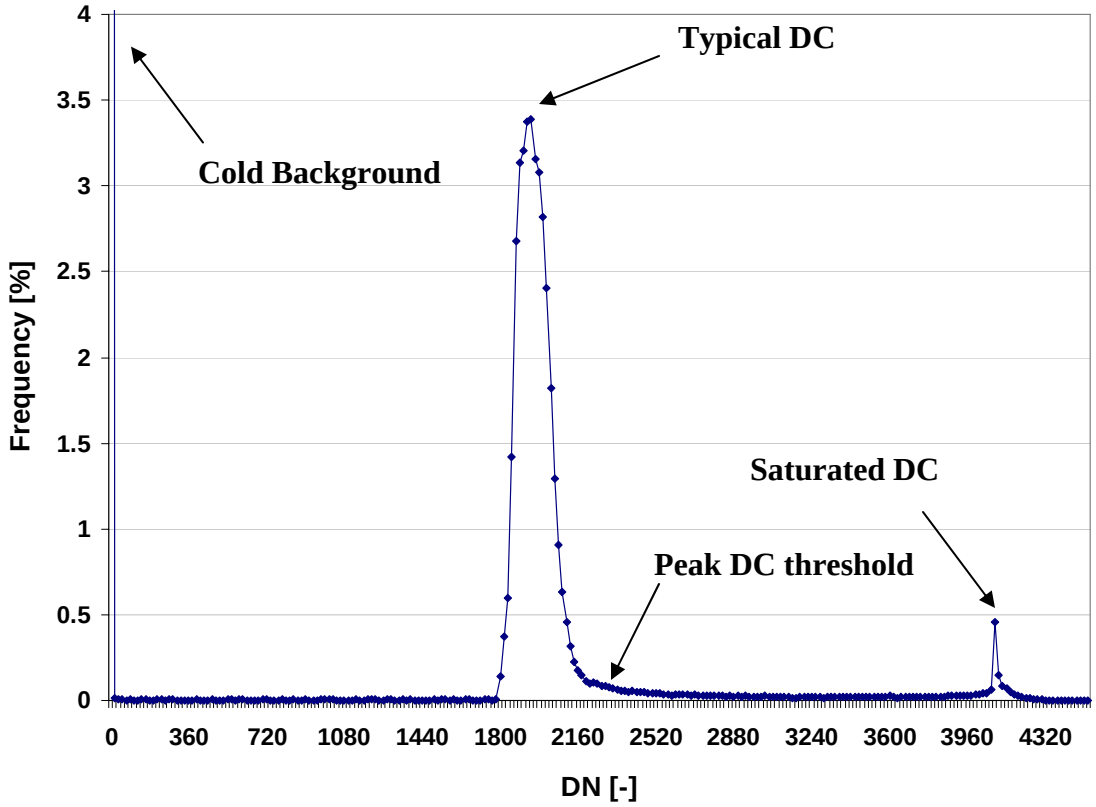

Figure 7. Single-image histogram

The histogram approach was used previously (Ononye et. al 2005) for identifying thresholds in bimodal distributions. In general, images from fire may show bi- or trimodal distributions, which was the case at Tar Hollow. In Figure 7, one subpopulation represents the cold background, another one indicates typical DC and a third one emphasizes saturation. The estimated peak DC threshold from each image using this approach was plotted in Figure 8. According to this plot, the true peak DC can fall between the threshold limit (triangles) and the saturation limit (doted line).

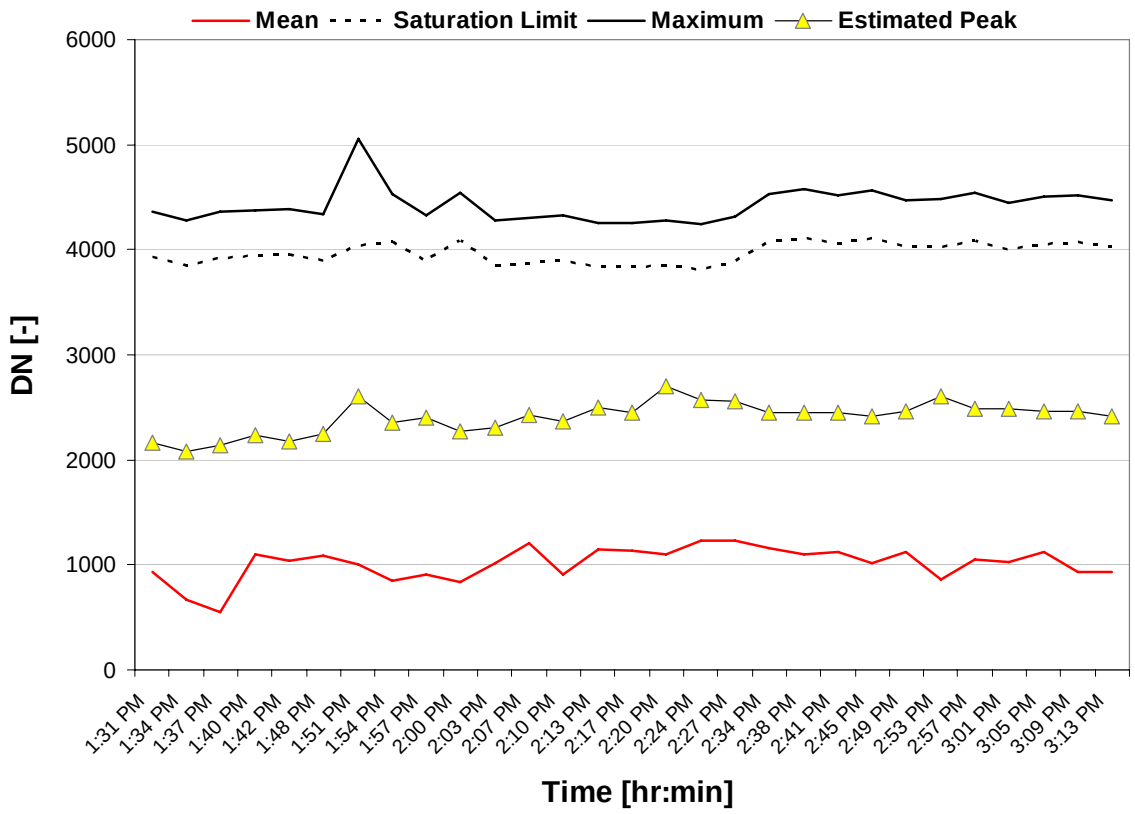

Figure 8. Estimated peak DC threshold for each time-sequence

Calculation of Fire Energy Release

Fire energy release in this study is a general term characterizing estimations of total heat release from two different data sets: calibrated (fire radiative power) and non-calibrated (row data/digital counts). At Arch Rock, fire emission was named fire radiative energy (FRE) because images were calibrated; at Tar Hollow, it was called time-integrated digital count (TIDC) because images were not calibrated. Determining the radiative energy from peak radiative power gives the upper bound of FRE. Conversely, if all pixels are used in estimation of FRE, the method gives the lower bound of FRE. The latter is a less accurate estimation because it does not consider the peak in radiative power and ignores the exponential cooling of the peak vs. time. Moreover, the time interval used to

integrate the radiative power at Arch Rock is not straightforward because of the gaps between IR images from fire; some peaks may not have been imaged or some peaks do not show cooling in time. Therefore, for accurate estimation of FRE, all FRP peaks identified with the help of firelines were numerically integrated using a trapezoidal rule to estimate FRE. It was assumed that after reaching a peak, radiative power cools down exponentially with time. The missing peak FRP values in the cooling curve (not imaged in infrared) were obtained via linear interpolation in both space and time and they were also included in the integration to prevent the underestimation of FRE. Then, as an attempt to derive an equation that can predict FRE from peak FRP cooling rates applicable to other fires, linear regression of ln (FRP) vs. time during cooling provided the cooling rate constant (slope from regression). A roughly similar approach to estimate TIDC from peaks was considered for Tar Hollow, but the possible missing peaks DC values were not included in the integration. Consequently, the TIDC range might be slightly underestimated.

Derivation of WB Variables

This study used the GIS-based water balance model of Dyer (2009) also available online at http://oak.cats.ohiou.edu/~dyer/water_balance.html. The toolbox was downloaded and applied for each study area to compute two important water balance (WB) variables, PET and AET. The schematic of the water balance model is presented in Figure 9.

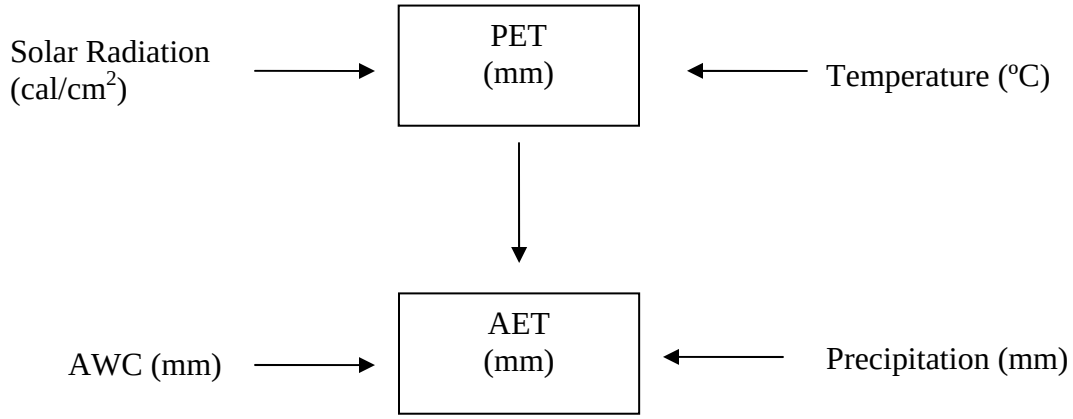

Figure 9: Conceptual water balance model

Both growing season PET and spring PET were computed with Equation 4 (Turc 1961). Growing season was defined as March-August 2003 (Arch Rock) and March-August 2006 (Tar Hollow). Spring season was defined as March-April 2004 (Arch Rock) and March-April 2007 (Tar Hollow). PET was computed for each month of the season, and then summed to give per season PET.

$$PET = 0.013 \cdot \left[\frac{T}{(T+15)} \right] \cdot \left[R_s + 30 \right] \quad (4)$$

where, PET = potential evapotranspiration (mm), T = normal monthly temperature (ºC), and R_s = monthly solar radiation (cal/cm^2).

A single monthly average temperature was considered for each study area. Solar radiation grids were estimated with the ArcGIS 9.3 Spatial Analyst Tools utilizing Area Solar Radiation. Radiation parameters Diffuse Proportion (D) and Transmittivity (T) were parameterized for each study area by running Points Solar Radiation for all possible combinations of D/T from D = 0.2 to 0.7 and T = 0.3 and 0.7, assuming a flat surface.

Then, solar radiation collected at a point within each study area was compared with solar radiation measured at Scalia Laboratory (Department of Geography, Ohio University, Athens, Ohio). D/T combinations having the smallest percentage difference in solar radiation were used to compute monthly solar radiation grids needed for PET determination. In this study it was assumed that incoming solar radiation in Athens did not differ appreciably from the solar radiation expected at Arch Rock and Tar Hollow. Arch Rock is within 40 km from Athens and Tar Hollow within 70 km.

The next step was to check if PET exceeded precipitation. Therefore, monthly average precipitation grids were prepared to compute the difference P-PET. If no deficit resulted (P-PET > 0), it could be assumed that PET = AET. If a deficit existed, AET (mm) was conditioned by the availability of actual soil moisture (storage) and precipitation (Mather 1968, Dyer 2009).

Storage grids were computed for each month starting with the month in which the difference between demand and supply (i.e., P-PET) was negative for the first time in the year, usually April or May. The previous month's "full" storage was equal to available water capacity. The current month's storage then became the input for the next month's storage and so forth. The difference between two months storage was then computed to be accounted for in the AET calculation; when [P-PET] is negative, plants supplement water available from precipitation by drawing upon soil moisture storage. If available moisture is insufficient to meet demand (i.e., if PET > AET), then a deficit exists. AET grids were used to infer productivity during growing season.

Assessing Relationships

Two research hypotheses were formulated in this study:

(1) AET can be related to fire energy due to its inferred relationship to productivity.

A relationship between energy released from fire and a surrogate measure of productivity (growing season AET) was expected because available fuel is considered as a direct driver of fire energy. Prior to relating productivity to fire energy, AET was tested against fuel measured as litter load (kg/m^2). AET was determined as the sum of six monthly grids that made up the growing season. Thus, the biomass (leaf litter) from the previous growing season could be assumed as fuel load for fire in spring. If a highly significant linear relationship was found between AET and measured fuel load, fire energy was tested against AET.

(2) PET, as a measure of water demand, can be related to fire energy due to its relationship to temperature and solar radiation; sites with high moisture demand are hypothesized to have low fuel moisture. The drier the fuel, the faster the fire and, therefore, the greater the heat released. Spring PET should therefore be an indicator of fuel moisture and should directly relate to fire energy. Additionally, a topographical analysis aims to support this hypothesis by means of indirect effect of aspect on fire energy release.

Statistical Tests Used to Evaluate Relationships

<u>Fire energy release vs. productivity (growing season AET)</u>

- Correlation of measured litter with AET at the pixel level

Values of growing season 2003 AET were determined at litter sampling locations within Arch Rock study area. Within Tar Hollow area, values of growing season 2006 AET were determined at randomly generated locations. The litter samples were located

about 2 km southwest from the burn unit, but within the Tar Hollow State Forest (Matthew Dickinson, personal communication 2009). Since this was the closest source of fuel measured in the field, it was assumed that it did not differ much from the fuel existing within the fire boundary because the forest composition is the same. Then, the two variables, litter load and AET, were plotted against each other to quantify correlation using scatter plots.

- Correlation of fire energy release with AET at the pixel level

Aside from testing the relationships litter load vs. AET and fire energy release vs. litter load, the relationship between energy release and AET was explored using similar scatter plots with data sampled at the pixel level.

- Correlation of fire energy release with AET at a coarser scale

This approach requires averaging the fire heat release by AET class. AET was classified in five classes using quantile breaks (Slocum et al. 2005); categories were representative of the AET distribution as informed by the histograms. Average fire energy release then was computed for each AET class. Average FRE was then plotted against the average AET for that class.

<u>Fire energy release vs. fuel moisture (spring PET)</u>

- Correlation of fire energy release with PET at the pixel level

In order to quantify a potential relationship between total energy released from fire and PET at the pixel level, the two variables were randomly sampled within both study sites. In an effort to capture general trends of fuel moisture and FRE aside from wind and ignition effects, pixel size was altered from 1 m to 3 m and 9 m at Arch Rock and from 3 m to 9 m and 27 m at Tar Hollow For each pixel size, random samples were

designed to extract FRE, TIDC and PET responses required for correlation and regression analyses (note that this operation was done for TIDC vs. AET at Tar Hollow using 100 pixels but not for FRE vs. AET at Arch Rock because it was found that both spring PET and growing season AET were highly correlated).

- Correlation of fire energy release with PET at a coarser scale

This approach is similar with the one described previously (fire energy release vs. productivity) using PET instead of AET. Spring PET was also classified in five classes according to data distribution using quantile breaks for both study sites.

- Topographical control by aspect

This additional analysis focused on two levels of information (mean FRE or TIDC and mean PET) in order to observe direct effects of aspect on fuel moisture and indirect effects of aspect on fire energy release. Therefore, aspect grids were derived from elevation for both study sites (Figure 10) using the Spatial Analyst tool in ArcGIS 9.3. The pixel size was 3 m for both study areas. FRE and PET pixels were extracted for each aspect category (see Figure 10) to compute means and to analyze trends using line or scatter plots.

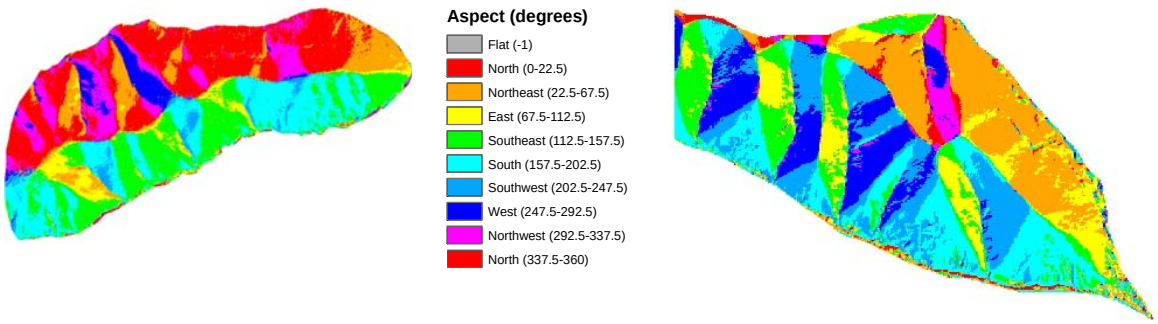

Figure 10. Aspect at Arch Rock (left) and Tar Hollow (right)

RESULTS

Firelines and Peak FRP

Firelines were used to observe the peak in radiative power at Arch Rock for more accurate estimation of radiative energy. In general, the peak occurred behind the fire front, in most of the cases within 2-4 m. There were peaks 1 or 8 m distant from firelines. In rare cases, the peak was on the line. The selected peaks from each image and the firelines are mapped in Figure 11.

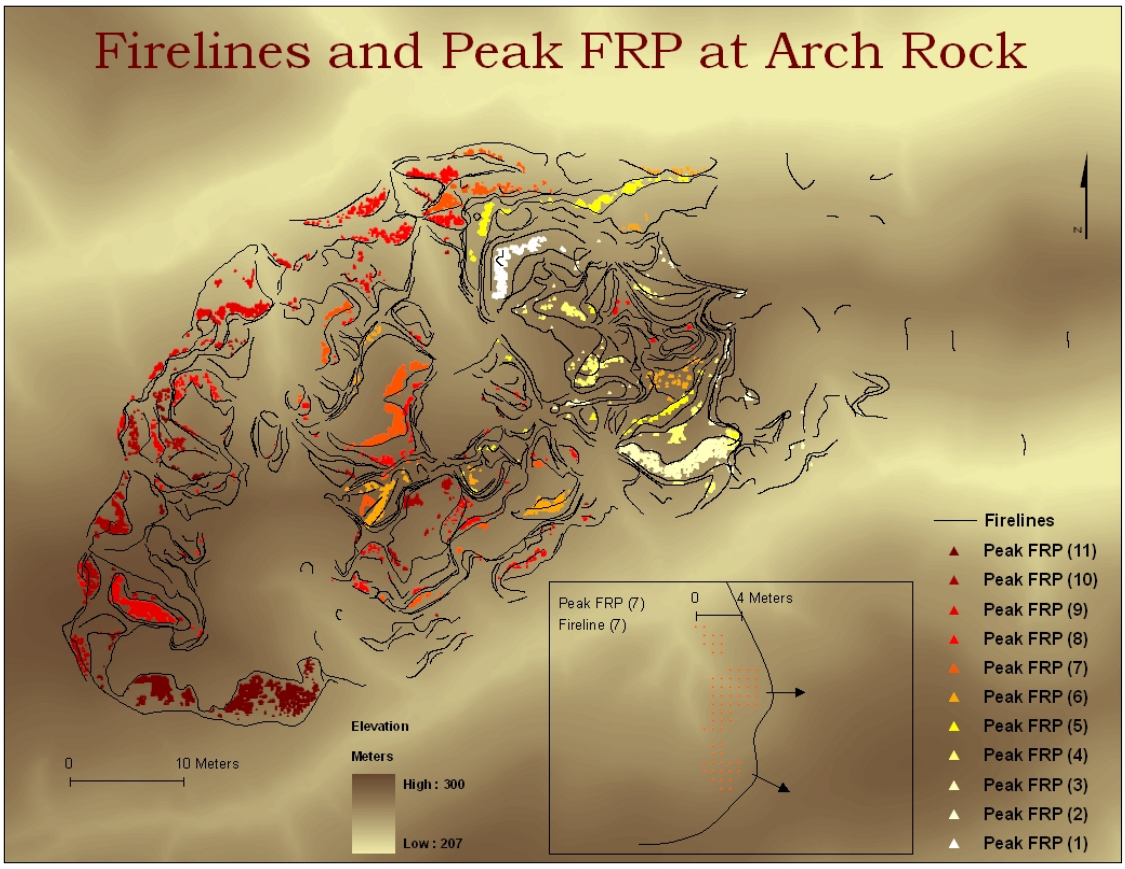

Figure 11. Fire features resulting from image segmentation.

Triangles are peak FRP of which color scheme symbolizes the progression from the first image (white) to the last image from fire (dark red). The inset provides a detail about the distance of peak FRP from fireline, while arrows are indicating the direction of propagation.

The time-sequence peak FRP has a relatively normal distribution as can be seen in Figure 12. Outliers were highlighted to observe the limits at which the distribution starts deviating from normal. The distribution is centered at 7.3 MW/m^2. Values below 3 MW/m^2 and above 9 MW/m^2 are extremes corresponding to unusually low and high values. These anomalies should not be included in the estimation of FRE .

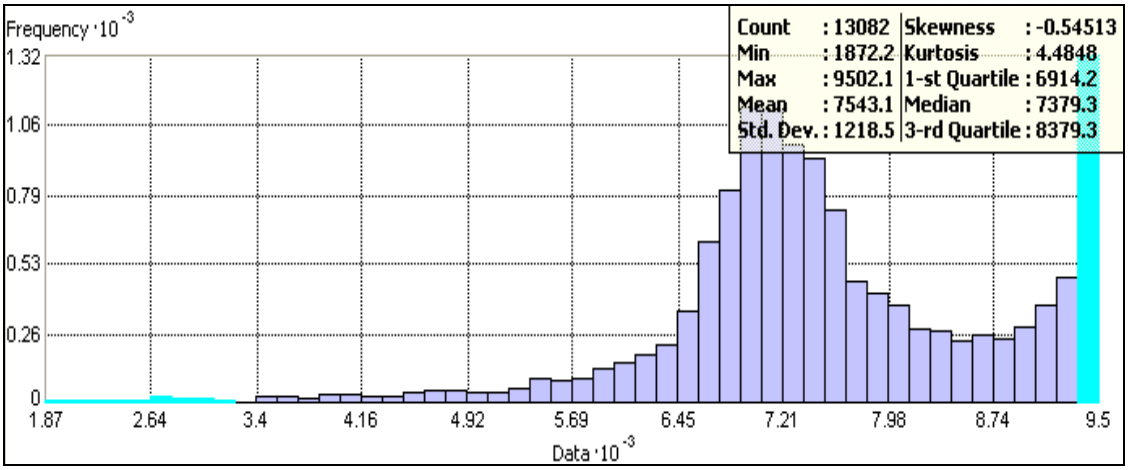

Figure 12. Histogram of peak fire radiative power at Arch Rock.

The spatial and temporal pattern of peak FRP mapped in Figure 13 emphasizes two clusters of saturated pixels in east (image 1) and west (image 11). Few scattered pixels were also noticed in the west (images 7, 8 and 9). Thirty-six unusually low peaks (< 3,000 W/m^2) were located in the east and center and only four in the west. The problem of saturation was more common in the west, where fire burned at higher temperature during the last three images from fire (images 9 to 11). The unusual cluster in the east may indicate that peak FRP might be caused by heat release from the diesel-gas mixture used for ignition. It is also possible that it was difficult to discriminate

between the real peak FRP and ignition with the method used in this study. The same argument can be made for the two saturated clusters in the west.

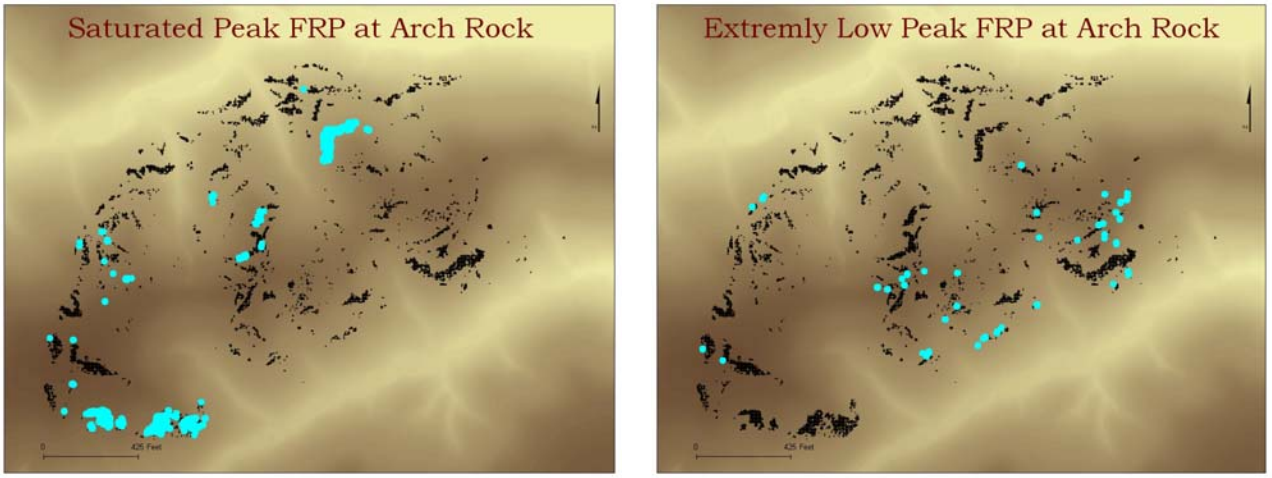

Figure 13. Outliers in the peak FRP distribution.
Black represents all peak FRP. Blue represents saturated peaks (left) and unusually low peaks (right).

In the case of Tar Hollow, the time-sequence peak DC was extracted using the previously established thresholds aided by the image histogram. Peak DC is normally distributed with median at 2.9×10^3 DC/m^2 as shown in Figure 14. The slight tail in the right is obviously caused by few observations above 4×10^3 DC/m^2.

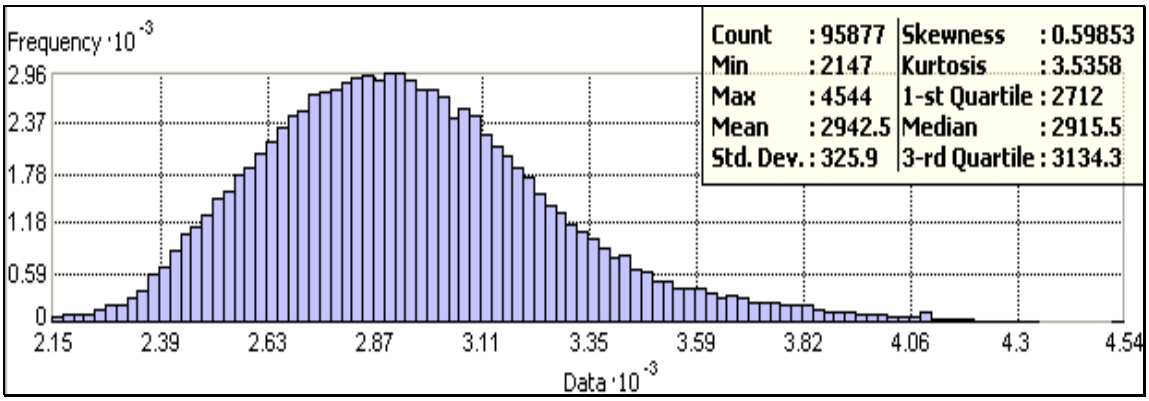

Figure 14. Histogram of peak DC at Tar Hollow.

The five time-sequence of peak DC mapped in Figure 15 shows where the peaks occurred in time and space.

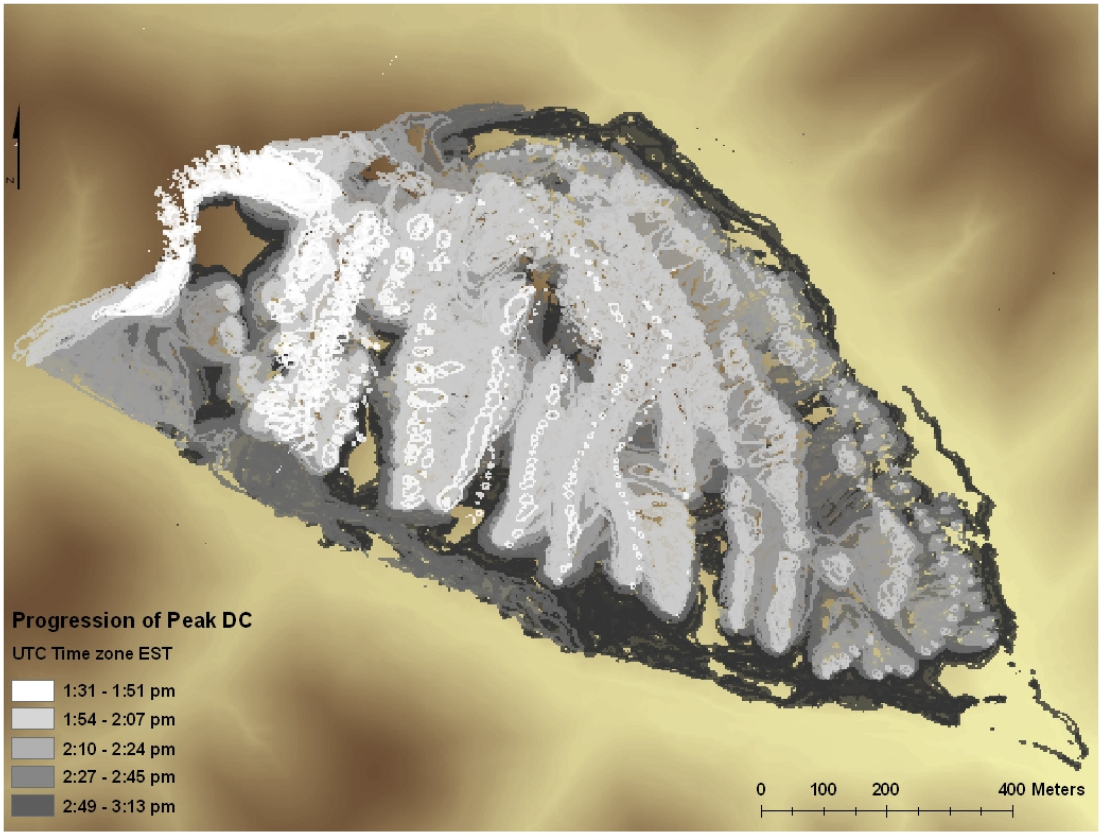

Figure 15. Map of peak DC by time-sequence at Tar Hollow.

About six or seven images were grouped to define a sequence in time (i.e., 1:31pm – 1:51 pm) from which the corresponding peak DC were extracted and mapped here. The grey color scheme symbolizes progression of the time-sequenced peak DC. White resembles the location of peak DC over 20 minutes from beginning of the fire, light grey the next 13 minutes, and so forth. The landscape mapped behind the peak DC pattern is elevation.

Fire Energy Release

Peak FRP at Arch Rock was numerically integrated to estimate FRE. Then, by knowing the duration of the cooling for each peak, linear regression of ln (peak FRP) vs. time during cooling provided the cooling rate constant (slope from regression). A power law

correlated the estimated FRE with the cooling rate in Equation 5 (numerical integration of FRE from peak FRP as well as Equation 5 are credited to V.L. Young as part of the Arch Rock pilot study):

$$FRE[kJ/m^2] = 104.88 \cdot (-slope)^{-0.65} \quad (5)$$

FRE pixels were aggregated to 3 m resolution to smooth the pattern (initial resolution was 1 m). The resulting FRE distribution is shown in Figure 16. Here, FRE units are MJ/m^2. Values above 13.5 MJ/m^2 were considered outliers and they are responsible for the large right tail of the histogram. A possible cause of these high FRE values could be isolated burning of large fuels (i.e., woody material) and heat release from ignition of diesel fuel. The distribution is centered on 3.8 MJ/m^2 (median). The resulting FRE range, excluding outliers, would be 1.7-13.5 MJ/m^2.

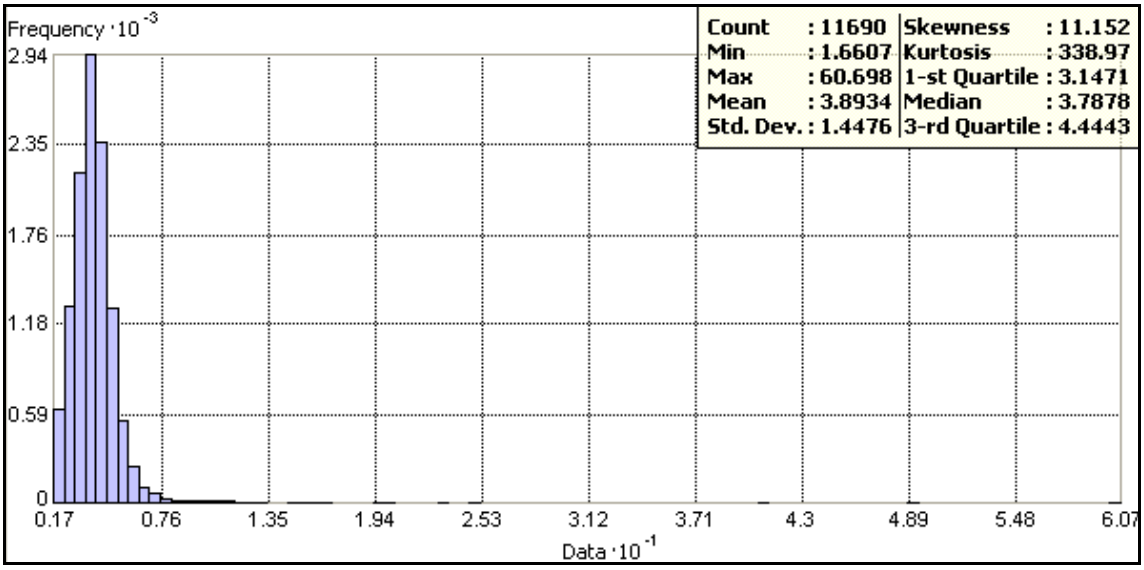

Figure 16. Histogram of FRE at Arch Rock.

Classified FRE according to the histogram was superimposed over spring PET in Figure 17. As expected, the northern slope has low PET (wetter fuel) and, therefore, fire released low heat (yellow pattern); on southern slopes fire released medium to high heat and PET indicated drier fuel. FRE values bellow 1.7 MJ/m^2 were not considered meaningful in terms of heat released from fire (i.e., background heat). Topographic breaks resulted in a fragmented fire pattern in particular on the north-facing slope but also on the south-facing slope.

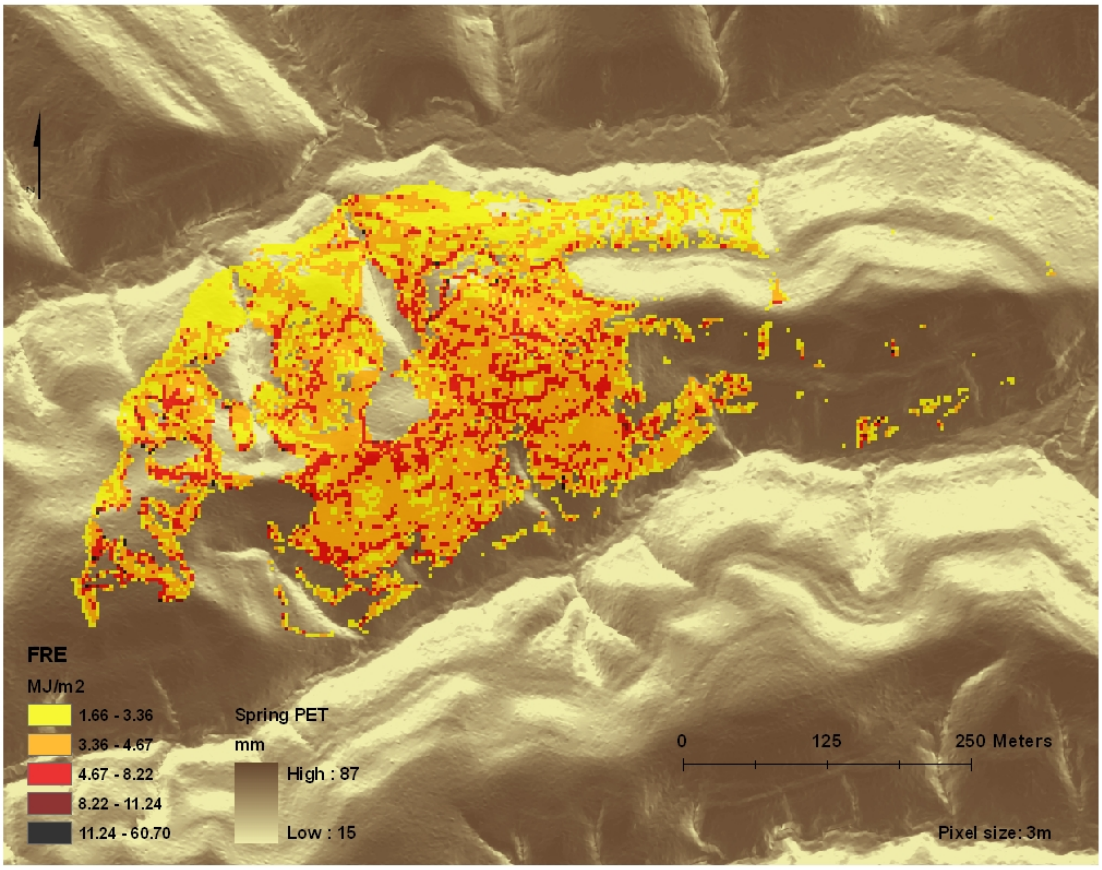

Figure 17. Total heat released from fire at Arch Rock Outliers (dark red) were included. Underlying landscape pattern represents spring PET. The intended overlay is to observe changes in heat pattern that might be caused by variations in PET.

For Tar Hollow, the energy released was estimated from peak DC at 3 m resolution using a similar method of integration as the one used for Arch Rock. Therefore, Equation 6 was applied in time intervals to estimate TIDC from two adjacent images. Then all integrals were summed to estimate total heat released.

$$TIDC = \int_{t_0}^{t_1} PeakDCdt \quad (6)$$

In Equation 6, TIDC is the time-integrated digital count, Peak DC is the peak digital count, and the difference between t and t_0 define the duration between two adjacent peaks. This method of integration provided a spatial pattern of TIDC at Tar Hollow of which distribution is shown in Figure 18. Units are MDC · sec/m^2. Its distribution has a log-normal appearance. Outliers above 230 [MDC · sec/m^2] were not included.

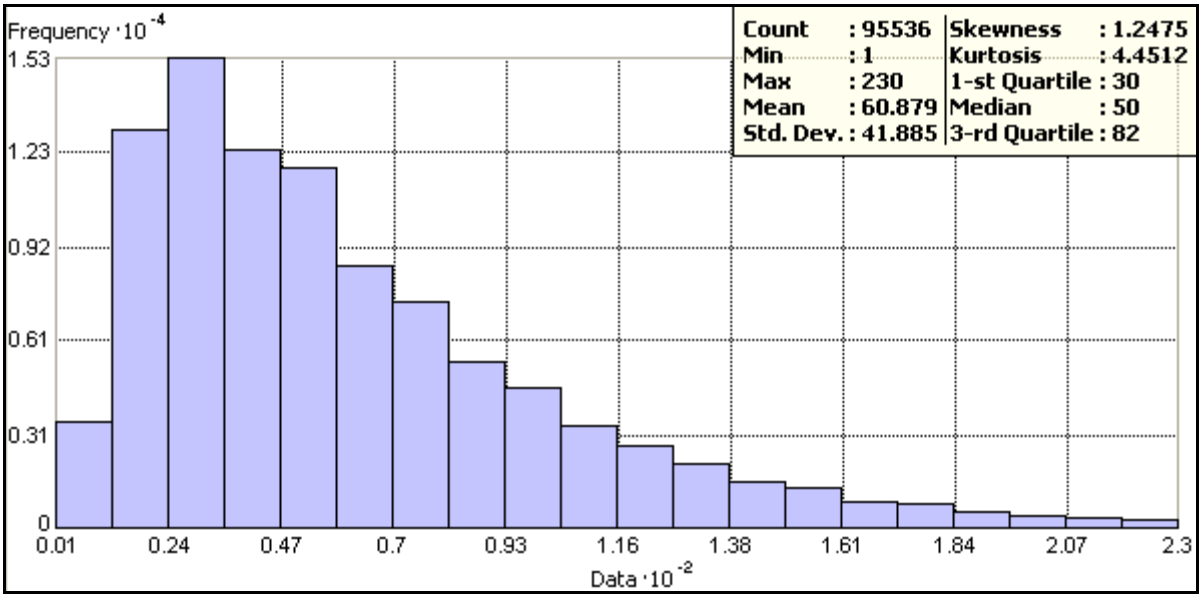

Figure 18. Histogram of TIDC at Tar Hollow.

Spring PET 2007 was used to map the underlying landscape in Figure 19. The superimposed TIDC pattern suggests that fire burned at higher temperature on slopes facing southwest and southeast and at lower temperature on slopes facing northeast. Spring PET ranged from 36 to 111 mm. TIDC ranged from 1 to 230 [MDC · sec/m^2]. Without calibration it is impossible to estimate what would be a reasonable limit of TIDC in terms of heat release. Topographic breaks correspond to fire pattern fragmentation on the southwest-facing slopes.

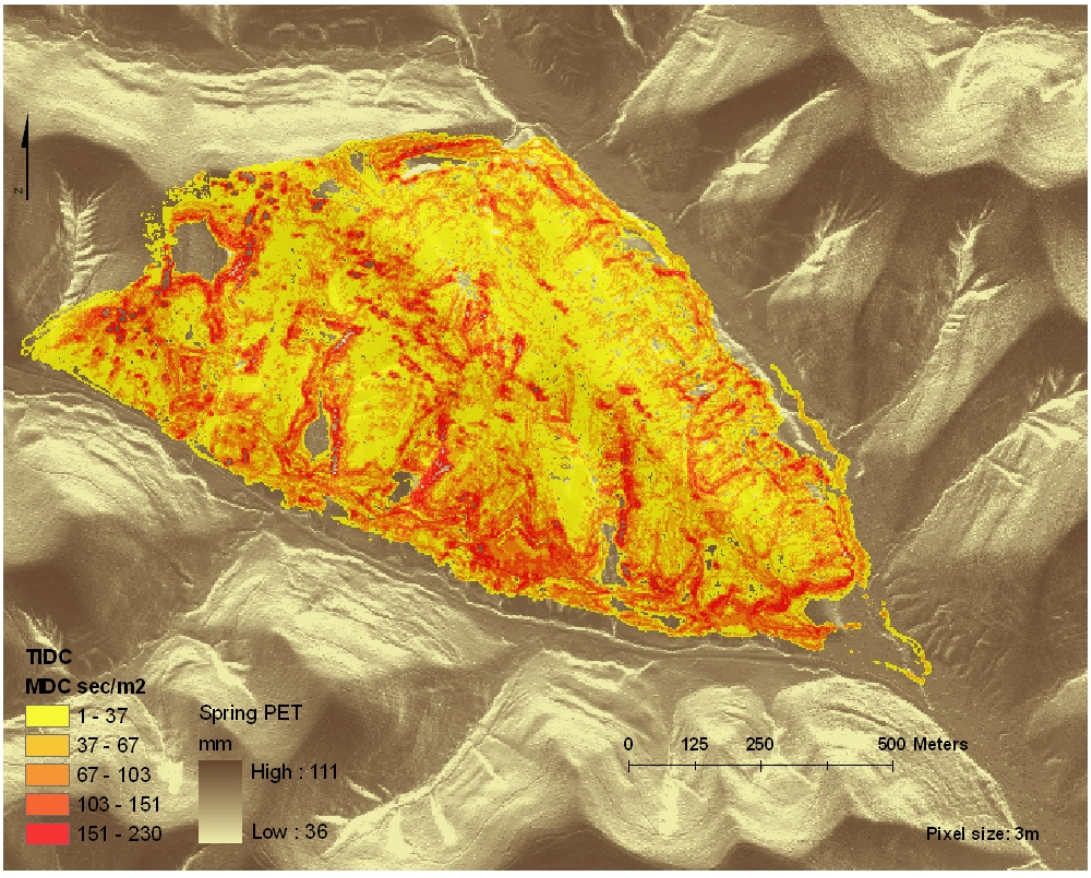

Figure 19. Total heat released from fire at Tar Hollow.

In parallel, as an attempt to derive a relationship that can predict TIDC from non-calibrated imagery, a random sample was used to extract pixels from each imaged peak DC and to observe for each pixel the time course of cooling using a roughly similar approach as the one developed for Arch Rock by V.L.Young. For the time period in which cooling was identified, peak DC was numerically integrated to estimate TIDC. In parallel, each selected pixel was transformed by natural logarithm in order to estimate the cooling rate constant assuming that after reaching the peak, DC is cooling down exponentially. Then, TIDC during cooling resulted from numerical integration was correlated with the cooling rate constant by a power law in Figure 20.

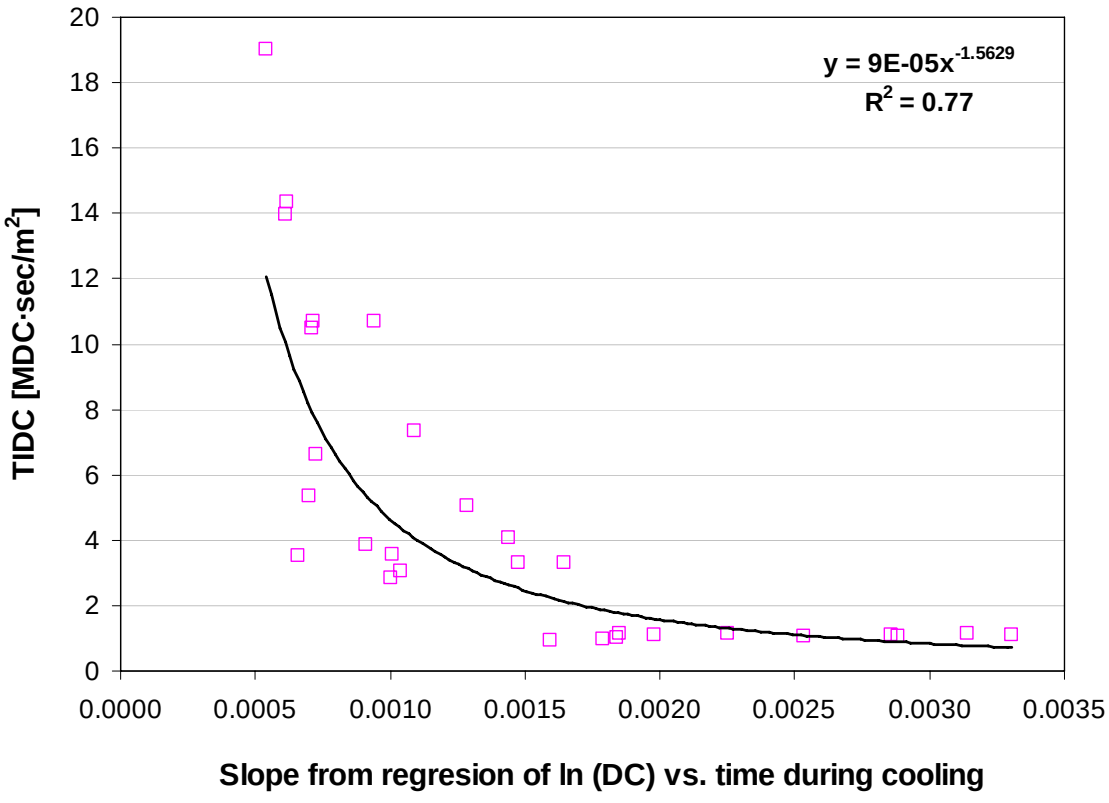

Figure 20. Correlation of TIDC vs. cooling rate of the peak DC.

This relationship derived from 30 data points is promising ($R^2 = 0.77$), but it requires a larger sample size to strengthen it. Notice that the relationship at Arch Rock was derived from more then 10,000 pixels and interpolation was used to account for peaks that were not imaged. The parameters of the power law model in Figure 20 are much smaller than the ones in Equation 5 mainly due to differences between the two data sets (calibrated vs. non-calibrated). An improved power fit for Tar Hollow can be applied to other non-calibrated fire data sets to estimate TIDC for a given range of slopes resulting from linear regression of ln (peak DC) vs. time.

Water Balance

AET was used as a surrogate measure of productivity during the growing season; the pattern is mapped in Figure 21 for Arch Rock suggesting that the topographic pattern is evident in the map of AET. PET was used to suggest fuel moisture in spring. In Figure 22, low fuel moisture is suggested on southern slope and high fuel moisture on northern slope.

Growing season AET at Tar Hollow mapped in Figure 23 shows a well-defined category with low values along the northwest-southeast ridge because of reduced AWC. Increased values predominate in the north and northeast where AWC was higher. The opposite pattern is depicted by PET in Figure 24. Here, low spring PET suggests high fuel moisture in the north and northeast and low fuel moisture in south and southwest. Low flammability is also suggested in the five coves in the southwest.

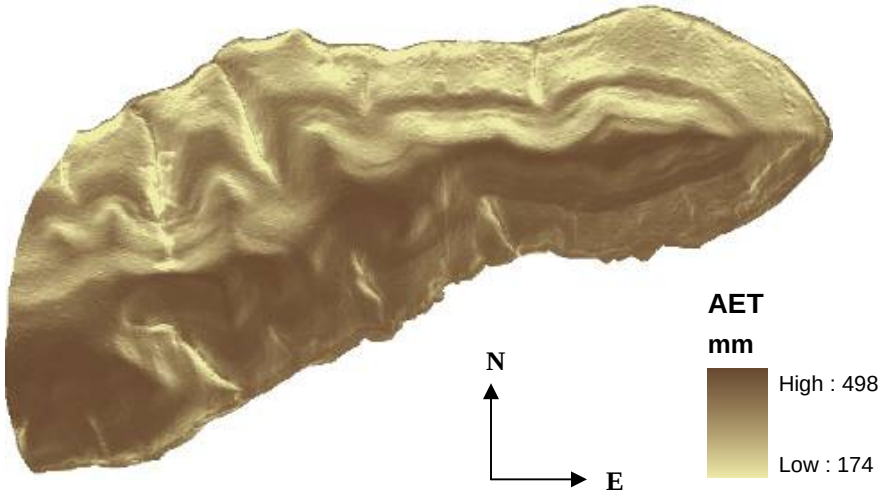

Figure 21. Growing season AET at Arch Rock.

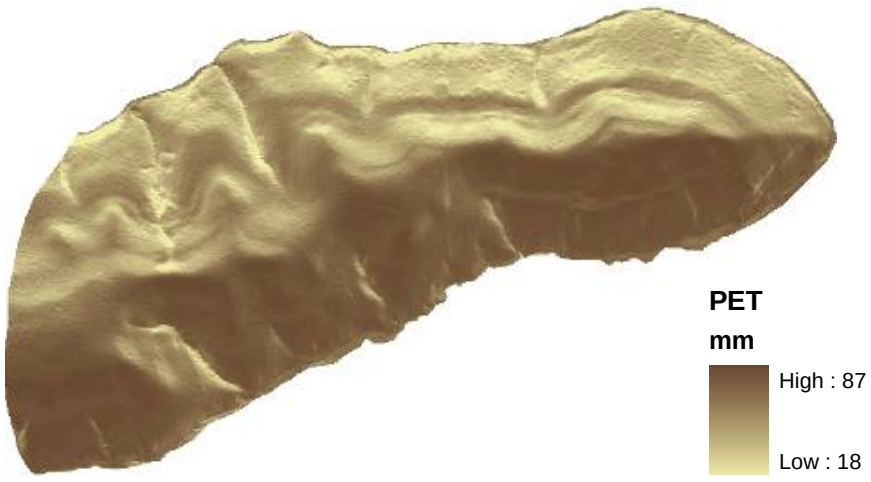

Figure 22. Spring PET at Arch Rock.

Figure 23. Growing season AET at Tar Hollow.

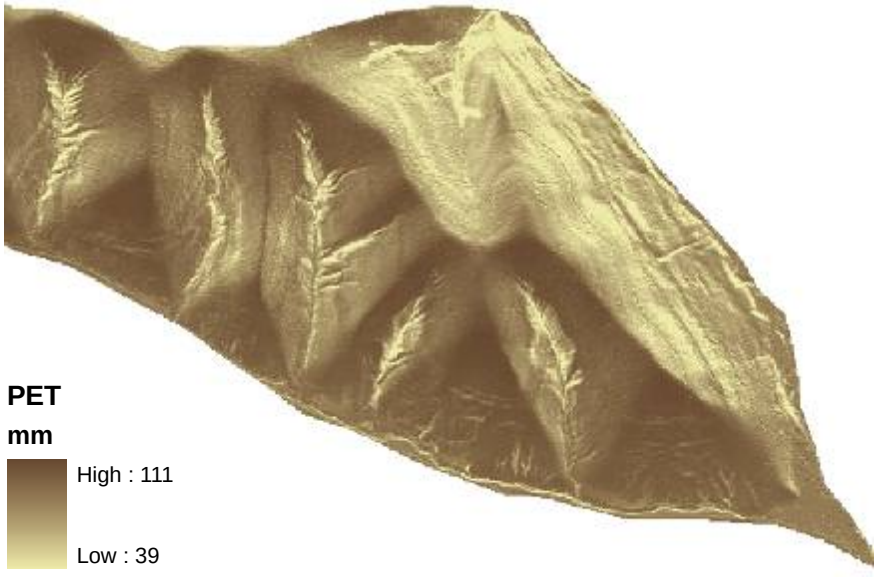

Figure 24. Spring PET at Tar Hollow.

Relationships

Fire energy release vs. productivity by AET at the pixel level

As hypothesized in this study, a relationship was expected between total heat from fire and productivity, inferred from growing season AET. A preliminary test was done to see if AET can be used to predict fire energy. Litter load was plotted against AET at Arch Rock (n = 40) in Figure 25, and against AET at Tar Hollow (n = 100) in Figure 26. Obviously, no relationships can be inferred given the large scatter in data points. However, fire was not fueled by litter only but also by artificial ignition, which can override "natural" controls. Averaging AET patterns by increasing pixel size from 3 to 9 meters did not result in a significant improvement of the scatter observed in Figures 25 and 26, suggesting that scale did not control the poor correlation of the two variables. However, no relationships were found between FRE and litter (Figure 27) or TIDC and litter (Figure 28). The fact that no relationship could be inferred between TIDC and litter in Figure 28 can be explain by the assumption made at Tar Hollow regarding litter sampling that it was done in the vicinity of the study area, but within the same forest having the same composition and, therefore, the same litter load. It is obvious that this assumption did not work. Similar outcomes, no relationships, were found in plots of FRE vs. AET (Figure 29) and TIDC vs. AET (Figure 30) using the same pixels.

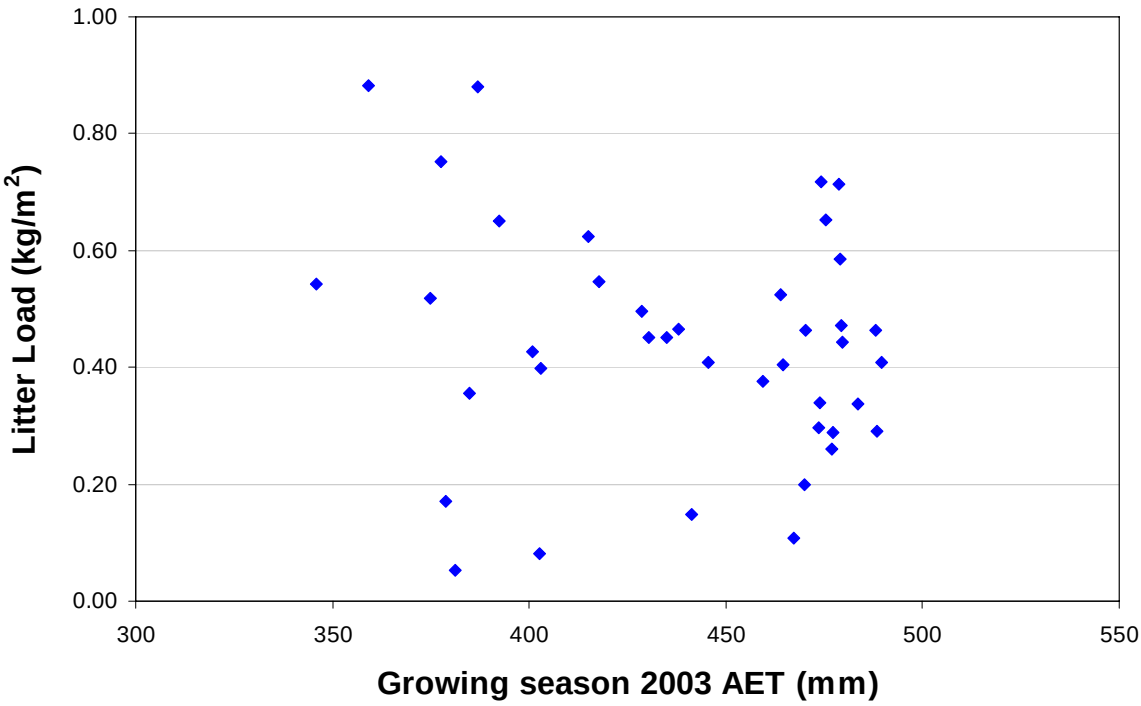

Figure 25. Scatter plot of litter and AET from 40 pixels at Arch Rock.

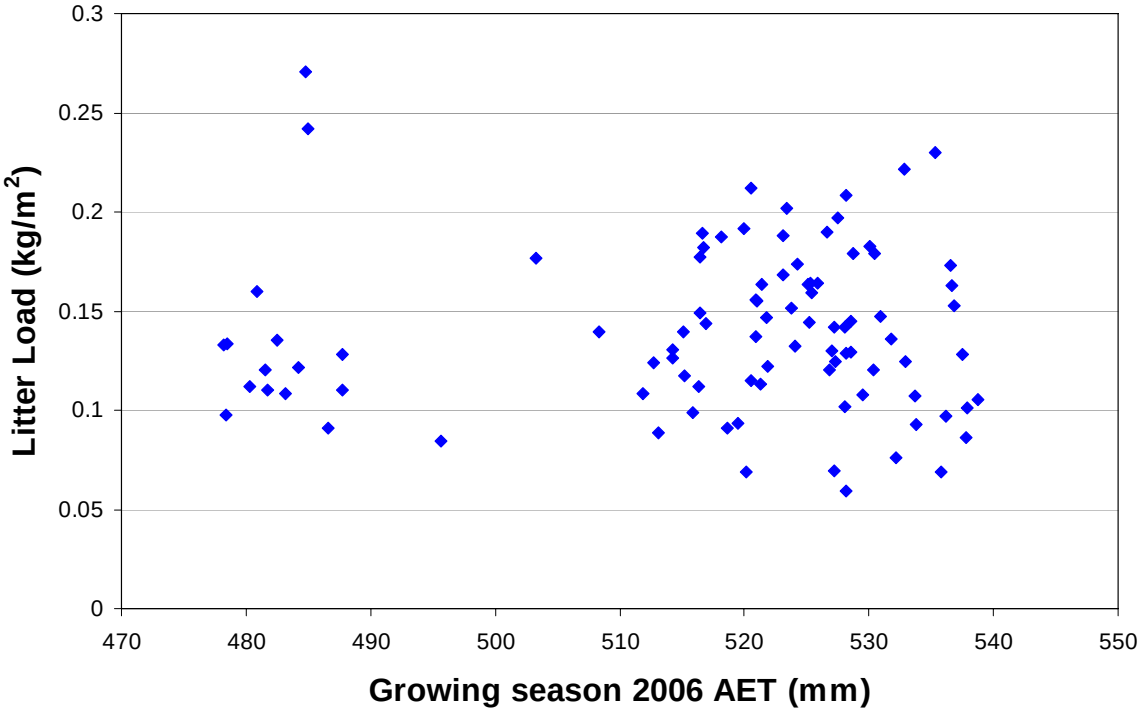

Figure 26. Scatter plot of litter and AET from 100 pixels at Tar Hollow.

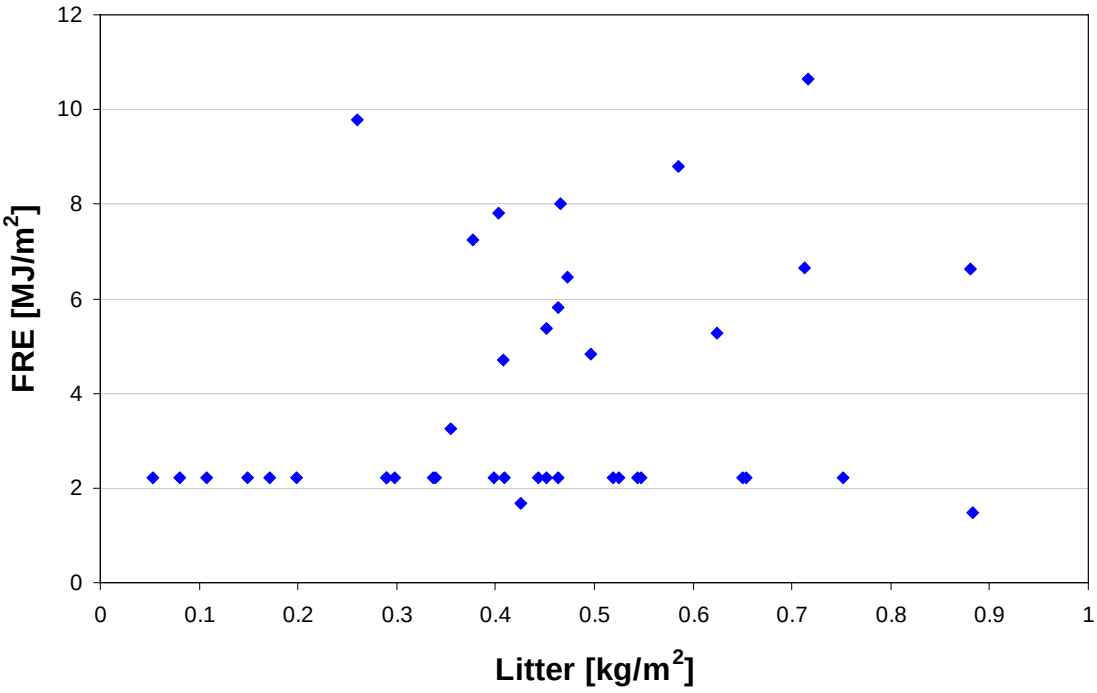

Figure 27. Scatter plot of FRE with litter from 40 pixels at Arch Rock.

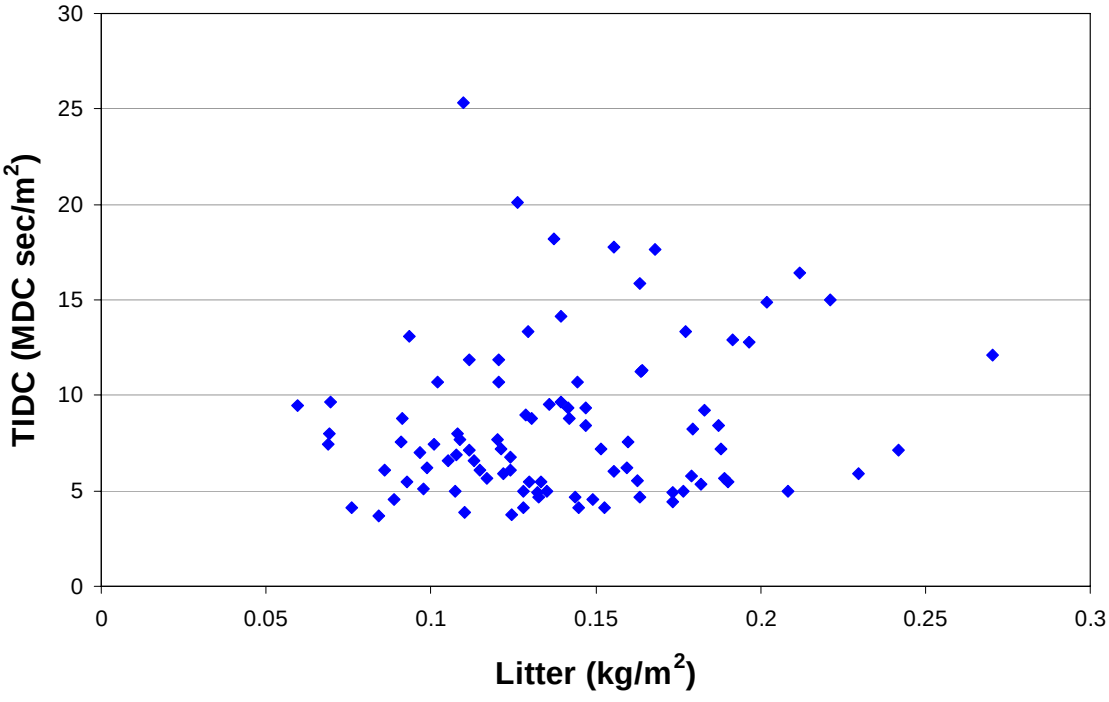

Figure 28. Scatter plot of TIDC with litter from 100 pixels at Tar Hollow.

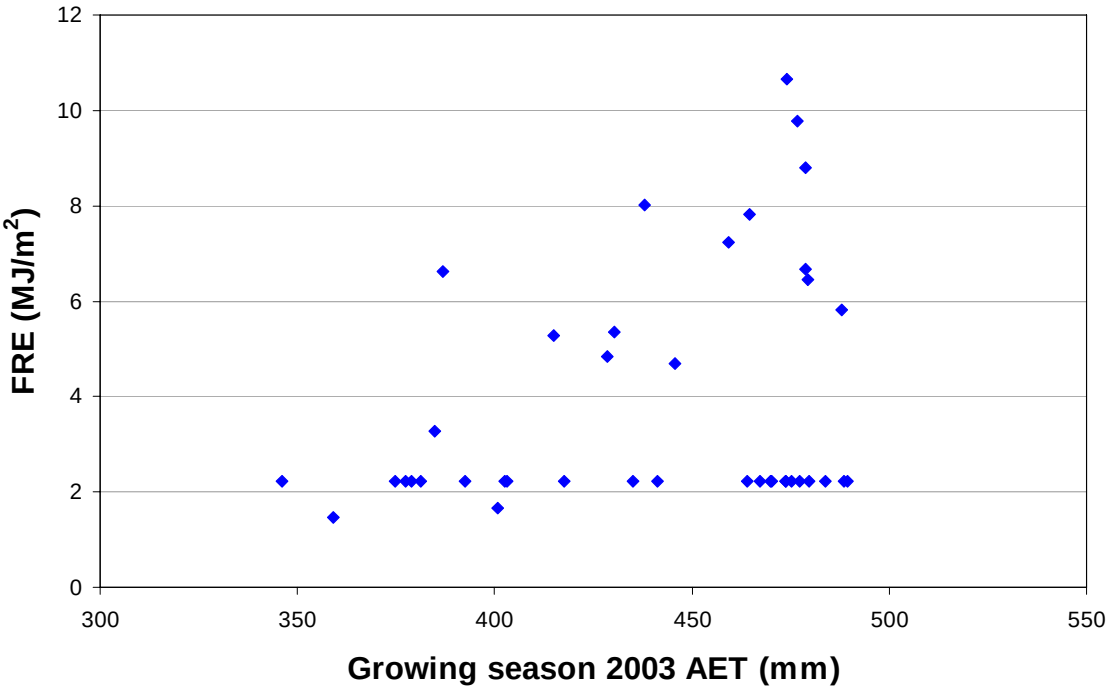

Figure 29. Scatter plot of FRE with AET from 40 pixels at Arch Rock.

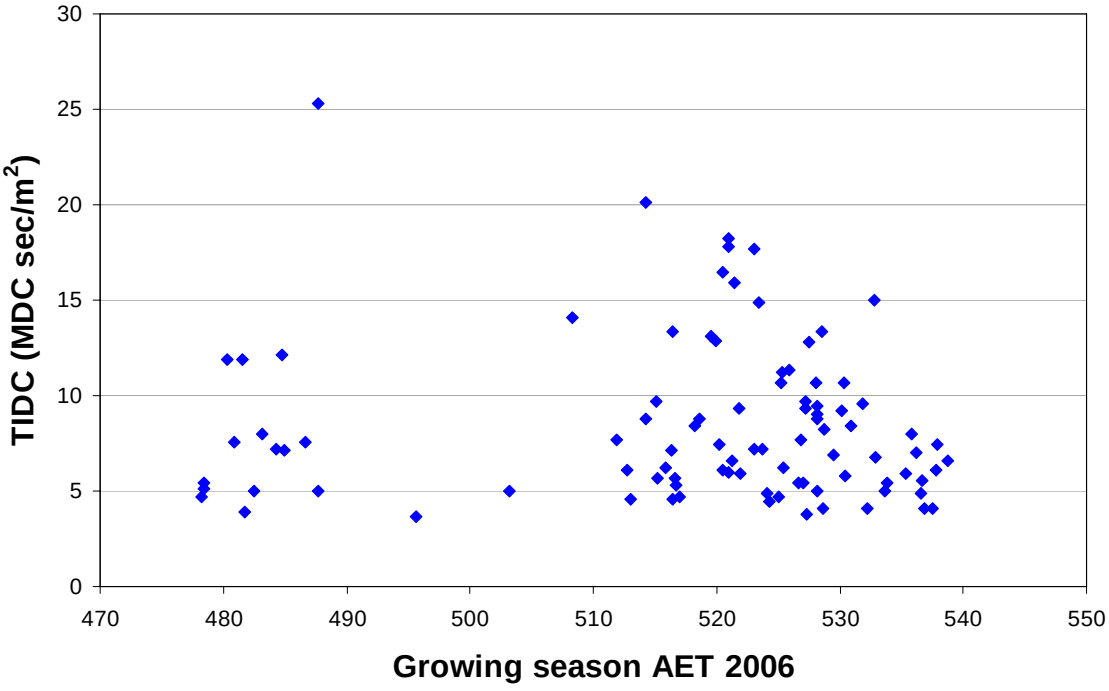

Figure 30. Scatter plot of TIDC with AET from 100 pixels at Arch Rock.

Fire energy release vs. productivity by AET at a coarser scale

When AET is used at a coarser scale (classes of AET) than the pixel level, it captures the response of fire energy release much better as shown in Figure 31 for Arch Rock. The error bars represent the 95% confidence interval for the mean. Data used to produce this scatter plot are presented in Table 1. The variability of FRE for each AET class is very small (± 0.05). The reduced FRE variability (y-error bars) indicates that the magnitude of FRE between each AET class (0.2 MJ/m^2) is significant.

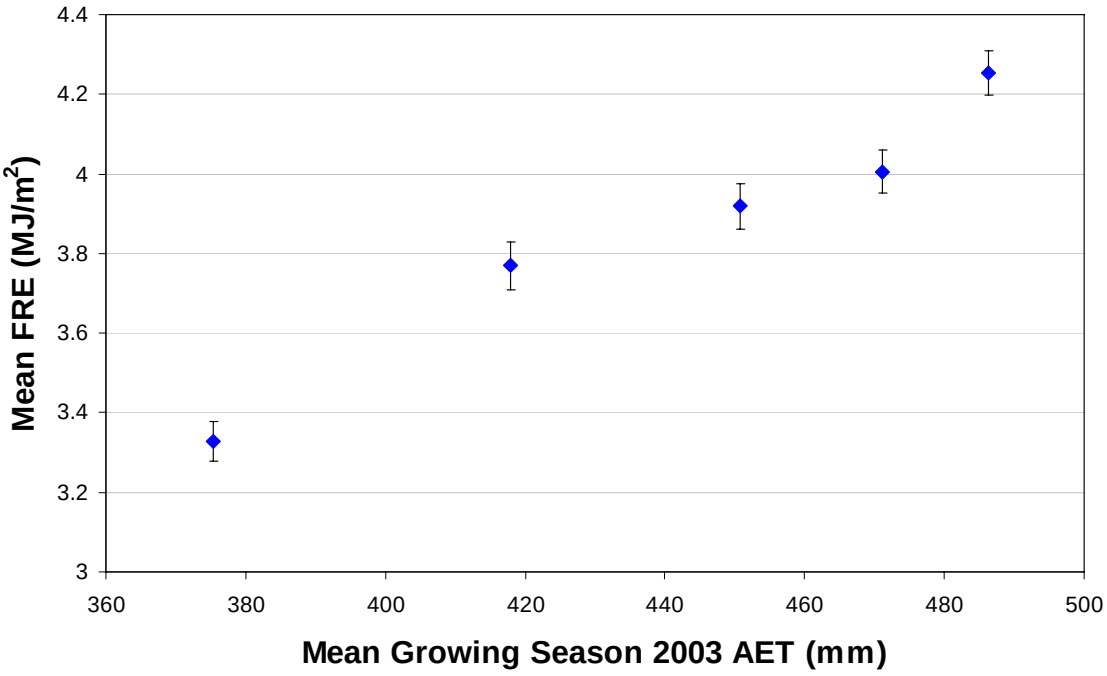

Figure 31. Coarse-scale scatter plot between FRE and AET at Arch Rock. Y-error bars are the 95% confidence interval for mean FRE. X-error bars are the 95% confidence interval for mean AET (they are to small to be seen at this scale).

Table 1

Descriptive statistics of classified growing season AET in relation to FRE at Arch Rock

Quantile Breaks	AET		FRE	
	Mean (mm)	95% confidence interval	Mean (MJ/m^2)	95% confidence interval
173.9 - 400.6	375.35	0.14	3.33	0.04
400.6 - 436.1	417.92	0.06	3.77	0.06
436.1 - 462.7	450.71	0.05	3.92	0.05
462.7 - 479.1	471.19	0.03	4.01	0.05
479.1 - 498.1	486.32	0.02	4.25	0.05

This analysis was repeated for Tar Hollow. In contrast to Arch Rock, no relationship could be inferred between AET and FRE (see Figure 32). Small variability on both axes suggests that the averages of the two variables are significant. Again, a quantile breaks classification scheme (Table 2) was used in this case to place AET observations in individual bins and extract the TIDC response accordingly.

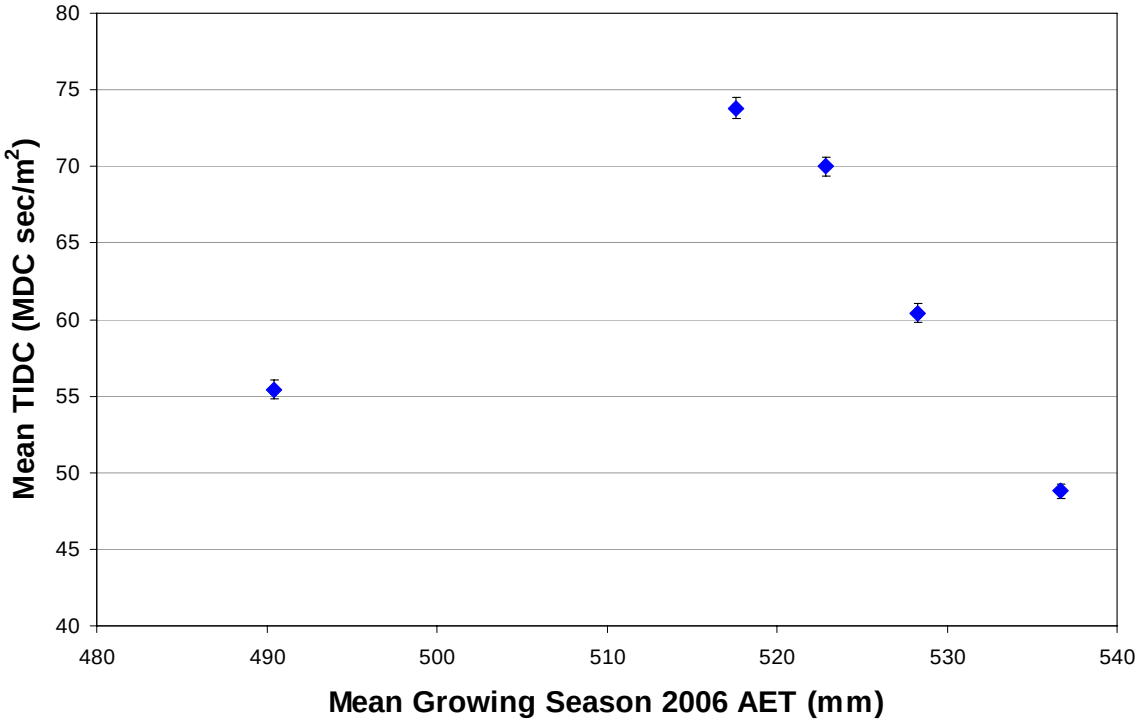

Figure 32. Coarse-scale scatter plot between TIDC and AET at Tar Hollow.

Table 2

Descriptive statistics of classified growing season AET in relation to TIDC at Tar Hollow

Qantile Breaks	AET		TIDC	
	Mean (mm)	95 % confidence interval	Mean (MDC sec /m^2)	95 % confidence interval
453.8 - 513.5	490.40	0.15	55.43	0.62
513.5 - 520.6	517.62	0.02	73.81	0.67
520.6 - 525.2	522.86	0.02	69.98	0.63
525.2 - 532.6	528.28	0.03	60.43	0.59
532.6 - 544.3	536.67	0.03	48.79	0.45

Fire energy release vs. PET at the pixel level

Fire energy and spring PET were randomly sampled at each pixel size (1, 3 and 9 m at Arch Rock and 3, 9 and 27 m at Tar Hollow). Similar analysis using scatter plots was done for each pixel size. Results confirmed that no significant relationship could be inferred by altering the pixel level. For exemplification, the scatter plot of data obtained at the 3m pixel level is presented in Figure 33. The sample size consisted of 243 data points. At Tar Hollow, results were similar. Figure 34 shows the scatter plot generated with 27 m pixel size data. Sample size was 1,318.

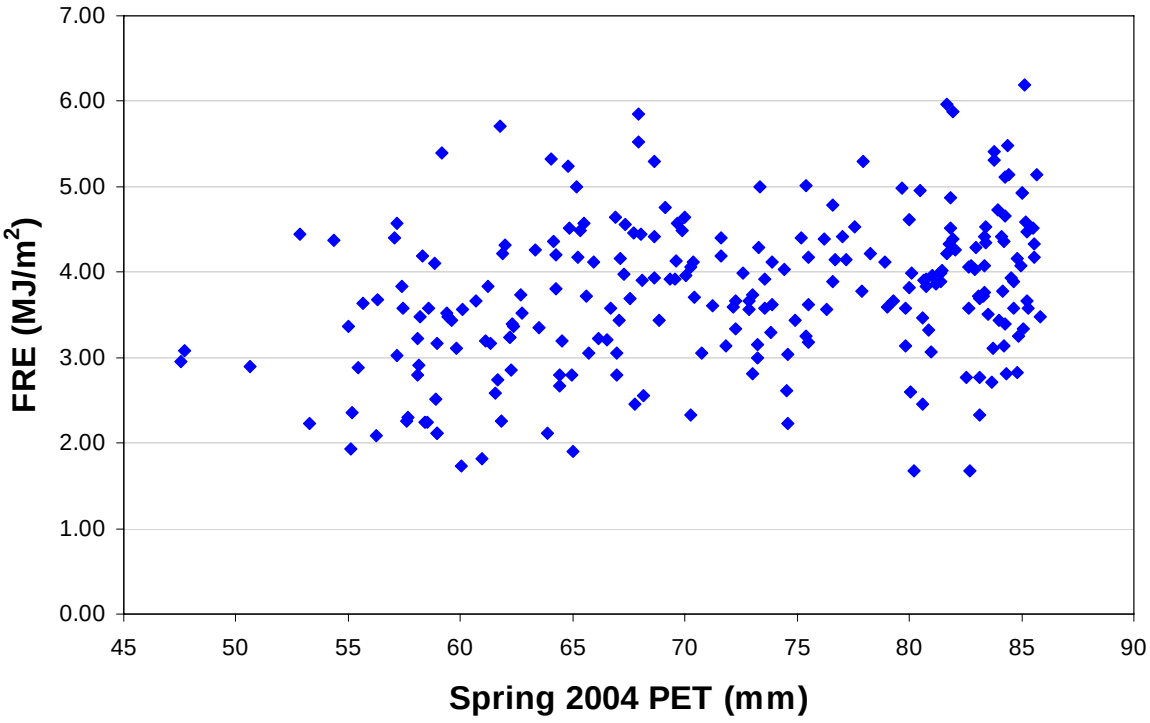

Figure 33. Scatter plot of FRE with AET from 243 pixels at Arch Rock.

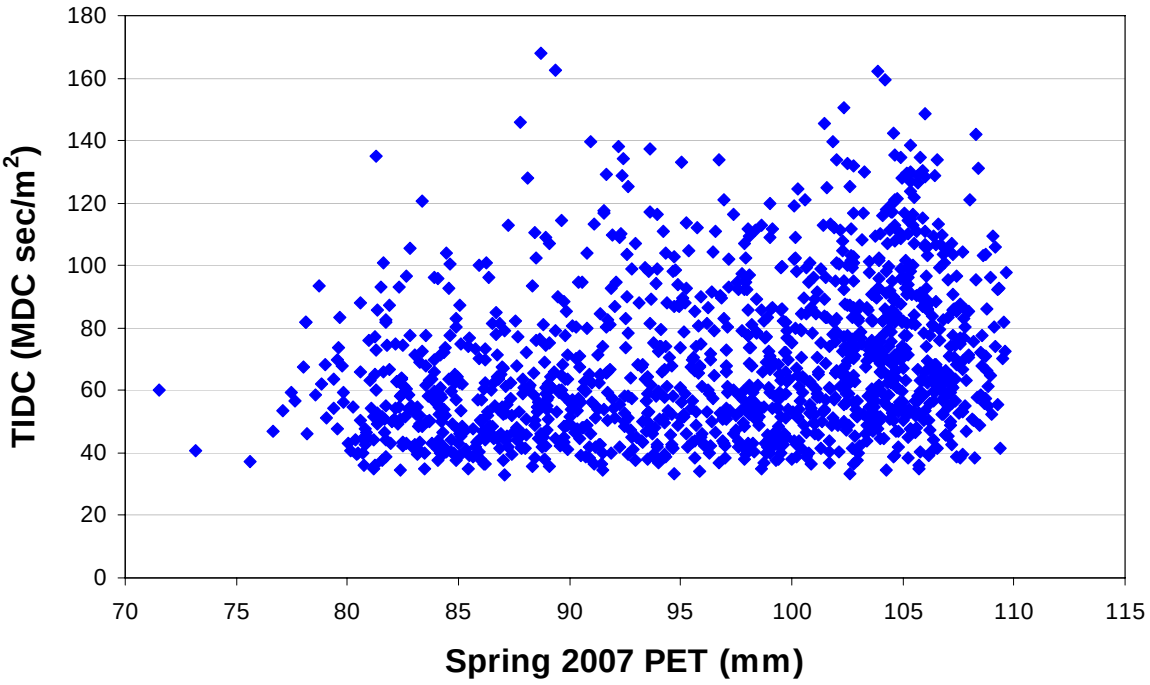

Figure 34. Scatter plot of TIDC with AET from 1,318 pixels at Tar Hollow.

Fire energy release vs. PET at a coarser scale

When classifying PET, the noise at the pixel level is reduced significantly by placing observations in representative classes of pixels. The mean FRE response to categorical PET shows a linear dependence on PET as inferred from Figure 35 at Arch Rock. Again, the error bars represent the 95% confidence interval for the mean. Table 3 introduces data used to generate the scatter plot. The variability of FRE for each PET class is very small (± 0.06). The magnitude of FRE between each PET class was 0.2 MJ/m^2. Small y-error bars indicate that this class difference is significant. X-error bars (± 0.02) indicate very low variability of PET. At Tar Hollow, variability of TIDC was a bit higher than at Arch Rock (± 0.6) because the area is three times larger, but also because of different fire behavior. PET shows a higher variability as well (± 0.5). Results are presented in Table 4 and Figure 36 for Tar Hollow.

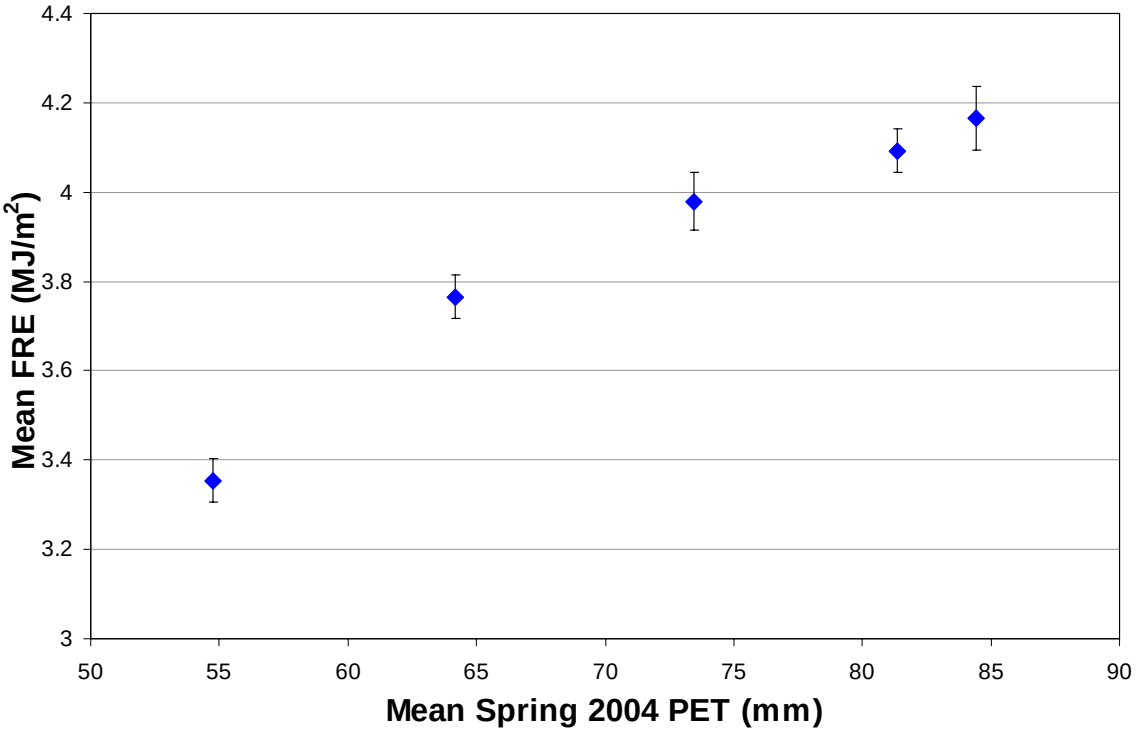

Figure 35. Coarse-scale scatter plot between FRE and PET at Arch Rock.

Table 3

Descriptive statistics of classified spring PET in relation to FRE at Arch Rock

Quantile Breaks	PET		FRE	
	Mean (mm)	95 % confidence interval	Mean (MJ/m^2)	95 % confidence interval
17.7 - 60.1	54.76	0.03	3.35	0.05
60.2 - 68.6	64.15	0.01	3.77	0.05
68.7 - 78.6	73.46	0.02	3.98	0.06
78.7 - 83.2	81.37	0.01	4.09	0.05
83.3 - 86.7	84.42	0.03	4.16	0.07

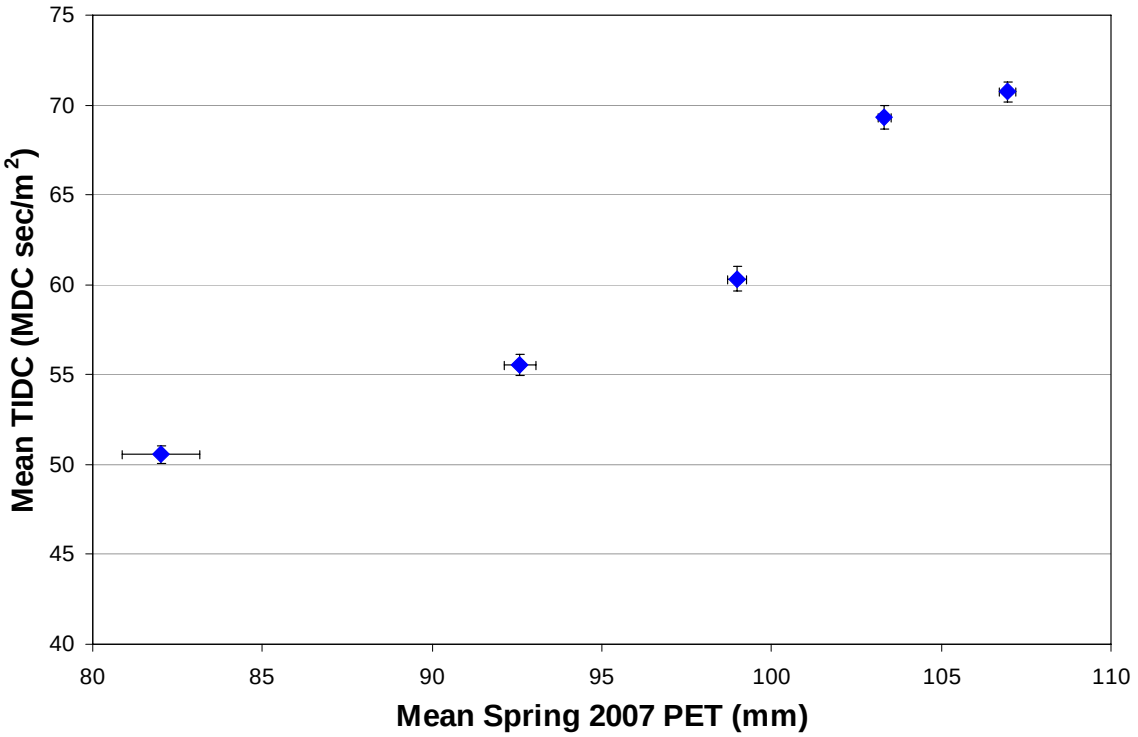

Figure 36. Coarse-scale scatter plot between TIDC and PET at Tar Hollow.

Table 4

Descriptive statistics of classified spring PET in relation to TIDC at Tar Hollow

Quantile Breaks	PET		TIDC	
	Mean (mm)	95 % confidence interval	Mean (MDC· sec/m^2)	95 % confidence interval
39.08 - 88.27	82.02	1.14	50.55	0.49
88.27 - 96.37	92.58	0.47	55.53	0.57
96.37 - 101.40	99.01	0.28	60.34	0.68
101.40 - 105.04	103.33	0.20	69.31	0.66
105.04 - 110.63	106.96	0.24	70.73	0.58

Topographical control by aspect

- Average trends of fire energy release and PET according to aspect

Means were computed for each variable (3 m resolution) extracted by aspect categories and plotted on the graphs in Figures 37 and 38. The lowest values in Figure 37 (109 mm and 5.6 MJ/m^2 respectively) were noticed on north-facing slopes. Conversely, the southern slope shows the highest mean PET (145 mm); the highest mean FRE was achieved on SW- and W-facing slopes (7 MJ/m^2). As error bars indicate, FRE has a higher variability than PET at Arch Rock, variability due to other factors than just fuel moisture and implicitly, aspect. Overall, the two means are consistent and a relationship can be inferred from these trends.

In Figure 38, fire energy seems to agree well with PET. Both means, TIDC and PET, reached the highest values in south (73 MDC sec/m^2 and 106 mm respectively) and the lowest values in northwest (47 MDC sec/m^2 and 88 mm). Here, even if aided by wind and aerial ignition, energy released from fire was more consistent with aspect, and therefore, fuel moisture. A better relationship between spring PET and fire energy can be inferred from these trends at Tar Hollow. Error bars indicate higher variability in TIDC than in PET, as observed at Arch Rock, but does not affect the obvious relationship between them with respect to aspect.

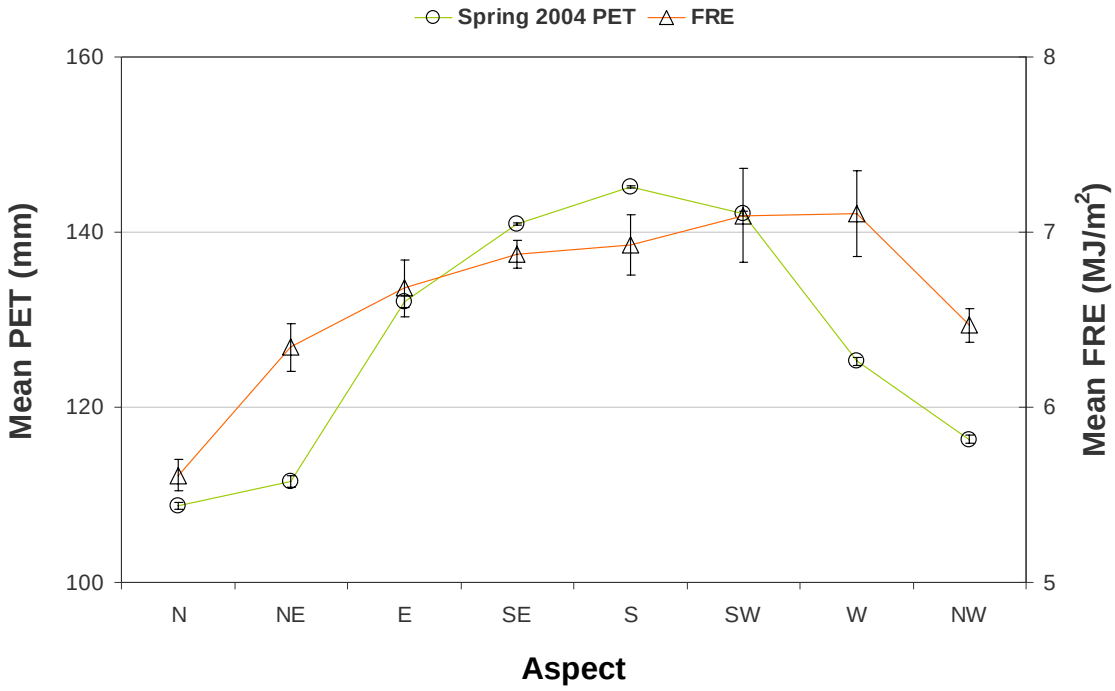

Figure 37. Average FRE and PET at each aspect.

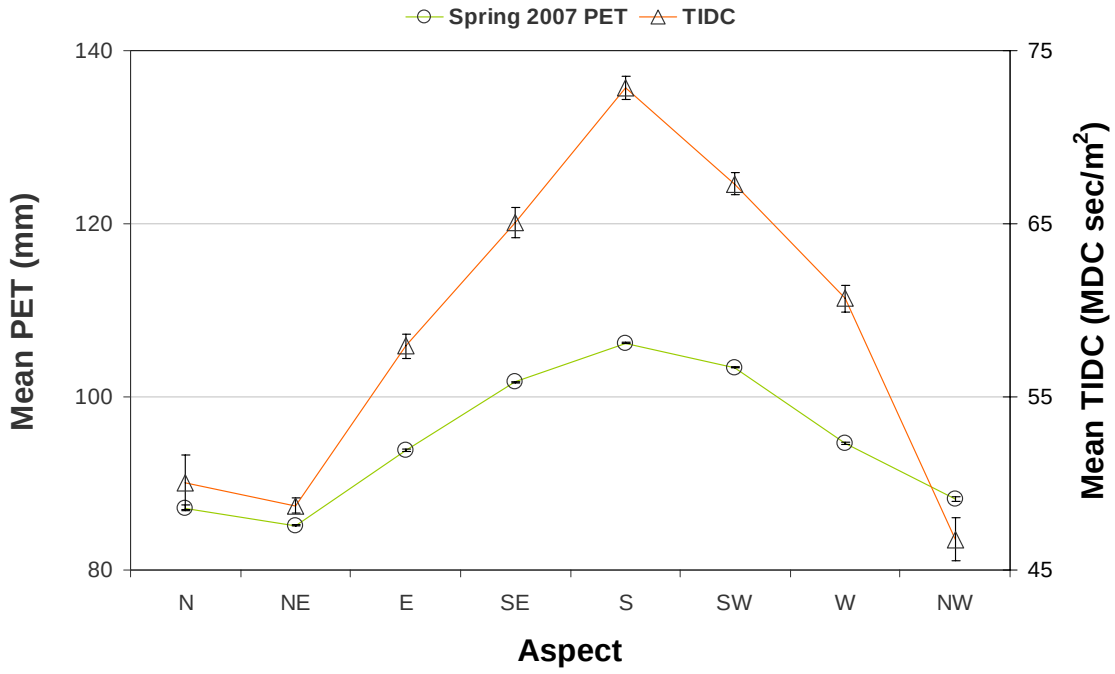

Figure 38. Average TIDC and PET at each aspect.

A scatter plot of mean FRE vs. mean PET was used in Figure 39 to observe the relationship inferred from Figure 37. Three clusters are obviously contributing to a linear relationship: one cluster grouped northerly aspect points with values of PET below 120 mm, a second one referred to an east-west exposure with values of PET between 130 and 138 mm, and a third one clustered points with southern exposure where PET reached 150 mm. Class variability by error bars indicates that FRE varied more in the west and southwest while PET varied more in the east and northeast.

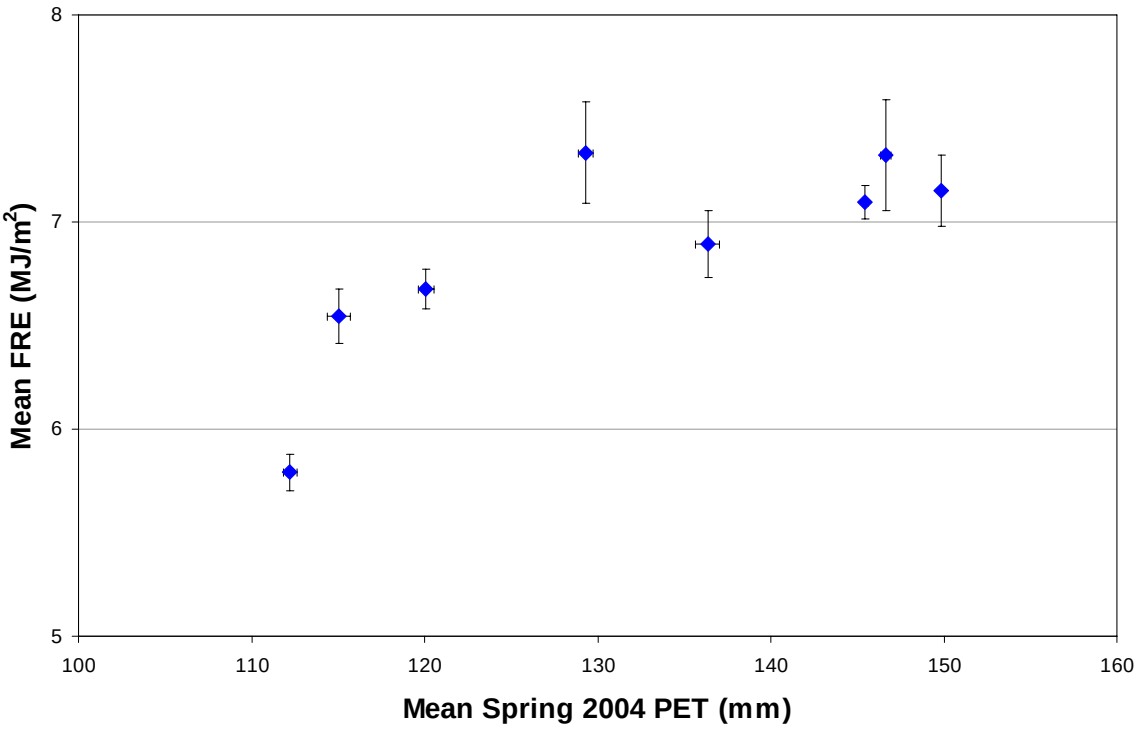

Figure 39. Relationship between FRE and PET according to aspect.

For Tar Hollow, a stronger linear relationship is suggested in Figure 40. Higher variability by both x- and y-error bars is apparent in the northern exposure group with values of PET below 90 mm.

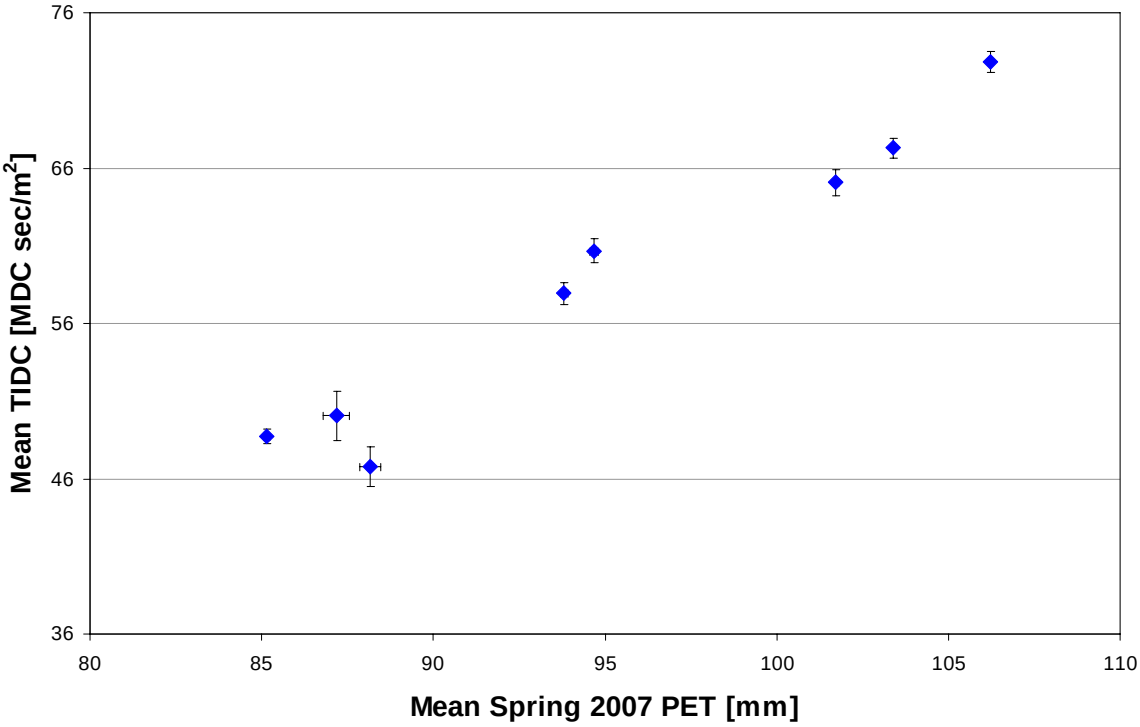

Figure 40. Relationship between TIDC and PET according to aspect.

DISCUSSION

Fire energy release

Firelines extracted in this study served to identify the peak in fire radiative power at Arch Rock with some limitations. Firelines did not work well in discriminating between backing and heading firelines. The major limitation considered was the fireline algorithm adapted from Ononye et al. (2007), which does not have a component that can separate between backing and heading peak FRP. A GIS approach was used in this study (Euclidean distance) to constrain the occurrence of the peak with respect of firelines. This approach assumed that the peak occurred behind the fireline (fire front) in a certain distance (2-8 m). The algorithm used to extract the firelines searched for pixels that were hot at the burn-not burn boundary for a given distance and it does not know how to discriminate between "hot backing" and "hot heading." In theory, distinction between backing and heading fires is straightforward (Davis 1959, Rothermel 1972, Smith and Wooster 2005, Viegas 2002), but geospatially it is difficult to estimate because it requires both expert knowledge and programming to write the algorithm that can make this discrimination from IR imagery. An alternative also tried in this study was to classify the firelines as backing and heading based on the direction of propagation: downward or upward. However, in reality this did not hold true everywhere on the landscape. Few attempts have been done for Arch Rock, but no significant results were found. Discrimination between backing and heading fires would help to select the peak FRP more realistically.

The peaks identified with this method were normally distributed with few outliers on both sides of distribution (low vs. high values). Saturation in IR signal was identified

responsible for outliers in the west (last images from fire when fire was very hot) and in the east (perhaps because of strong ignition in the first image from fire).

Peak selection from non-calibrated data (digital count) at Tar Hollow used a different method, image histogram to establish thresholds. The extracted peaks were normally distributed and biased towards extreme high values because of saturation. The Tar Hollow data set was much more saturated than Arch Rock because of the nature of the fire and a lower dynamic range of the instrument used at Tar Hollow.

Finally, fire energy release was estimated from peak radiative power (Arch Rock) and peak digital count (Tar Hollow). The two estimations could not be compared but their spatial patterns could be explored geographically. Calibration does not change the pattern (TIDC is related to FRE by a constant). FRE at 3 m resolution resulted in the expected range of a low intensity fire of which typical value was 3.6 MJ/m^2. This corresponds to a total fuel consumption of roughly 1.3 kg/m^2. The typical TIDC value was 50.4 $MDC \cdot sec/m^2$. Typical consumption could not be estimated for Tar Hollow because TIDC was derived from non-calibrated data. Efforts to predict fire energy from non-calibrated data are ongoing at Tar Hollow aside from the goals of this thesis. However, this study also attempted to derive a relationship following the method developed for Arch Rock. The power law fit, if improved by including in the integration the missing peak DC on the cooling curve can be used to predict energy released from non-calibrated data. Overall, the first goal of this study, estimating fire energy release, was successful within the limitations of both data and methodology.

Growing season AET and fire energy release

The water budget was used in this study to estimate AET as a surrogate variable for productivity in two different physical and temporal contexts (Arch Rock – growing season 2003 and Tar Hollow – growing season 2006). The fact that AET did not correlate with litter measurements at the pixel level raised concerns about data quality. One explanation might be that measured litter did not represent well the range of the fuel available at the site (i.e. the assumption for Tar Hollow about litter sampled outside the fire unit). At Arch Rock, litter load was measured within the fire unit and still the relationship does not hold at the pixel level. There was also no relationship between litter measurements and the estimated heat released from the fire, which might suggest that litter measurements taken at 40 sites are note adequate to assess site conditions. If litter measurements are reliable, the problem might be the scale at which these relationships are being analyzed or other local factors. Factors that may obfuscate the relationship include local interactions between rainfall before the fire which may have influenced fuel moisture and, consequently, fire energy release (more likely the case of smoldering combustion, low fire-temperature and, therefore, low thermal signal measured in infrared), soil moisture dynamics (in- and out-moisture flows from the ground), variation in decomposition rates (xeric sites have lower decomposition rates than mesic sites), and litter quality (species-specific variations in decomposition rates associated with different topographic sites). Productivity is only one side of a litter mass budget where litter load = litter produced - litter decomposed (Mathew Dickinson, personal communication 2009). Therefore, AET could not predict FRE or TIDC at the pixel level. In contrast, when focusing on classes of AET, which account for a coarser scale of analysis than the pixel

level, FRE responded very well to AET at Arch Rock. Using a similar analysis at Tar Hollow, this change in scale of AET did not provide a relationship between TIDC and AET similar to Arch Rock. The initial reaction is to blame TIDC for this finding (the estimation underestimated TIDC and included saturated values). However, at a similar scale of analysis TIDC proved to be reliable in relation to PET (discussed below). Alternatively one may question AET (estimation included PET, precipitation, and AWC), although it proved to be a reliable measure of moisture use by plants (it compares storage with soil moisture).

Spring PET and fire energy release

Another aspect of the water budget, PET, was used to infer fuel moisture of a site and explore its potential to explain FRE. Spring 2004 PET was computed at Arch Rock and spring 2007 PET at Tar Hollow. The analysis of PET vs. fire energy release at the pixel level using scatter plots was not successful although the size of the pixel was altered at both study sites.

As seen previously with AET at the pixel level, it is rather a question of how fine the scale of analysis should be in order to see a significant relationship. It is obvious that a pixel level is too fine. It should kept in mind that fire energy release was measured in infrared from two small controlled burns. A pixel-phenomenon is more characteristic of large wildfires monitored from satellites.

By increasing the scale of observations via categorical PET, results supported the hypothesized relationship between spring PET and fire energy release. The linear relationship inferred at Arch Rock was stronger than the one obtained at Tar Hollow, pointing out again the difference between fires in terms of ignition but also weather

conditions. Class variability in PET at Tar Hollow was higher at small values (< 90mm) suggesting high fuel moisture. At Arch Rock, variability of PET was very small in all classes.

Aspect, spring PET and fire energy release

Aspect proved to be important for both fire energy and spring PET. FRE was more variable than TIDC according to aspect. This difference might be resulting from differences in sample size, but also from different fire behaviors. The Tar Hollow fire was ignited by many point ignitions, whereas Arch Rock was primarily ignited by a few ignition lines. Tar Hollow ignition pattern would have better “sampled”" the fuels at Tar Hollow, allowing fuel effects to express themselves more fully. At Arch Rock, weather conditions were also marginal (recent rain, higher relative humidity on the burn day), probably masking not only topographic but also microclimatic controls on fire behavior, two main concerns of this study. However, as previous studies agreed (Bennie et al. 2008, Dyer 2009, Turc 1961), aspect is one important driving force of solar radiation and through its effect on PET therefore influences moisture gradients. PET influences fuel moisture at a landscape scale and consequently factors into fire behavior expressed in this study as fire energy release. Any deviation of the mean response in fire energy release from the mean response in PET by aspect indicates other causes than fuel moisture, such as additional ignition (i.e., other fuel) and wind. The agreement between two mean responses by aspect is qualitative only. In addition, some of the variation in the range of FRE, TIDC and PET was smoothed by averaging values from pixels for each aspect. However, hydrologically-determined variation in fuel moisture occurs at finer spatial scales than categorical aspect.

CONCLUSION

The thermal response from fire was measured in infrared to estimate total energy using methods specific to remote sensing and image analysis. The method of estimating heat release from fire in this study is applicable to other fires. This study provides two different methods for peak radiance identification that can work for calibrated and non-calibrated data sets. However, it is pointed out that missing digital information from fires should not be ignored in the final estimation of heat release. Another application could be the estimation of total fuel consumption using established relationships between fire radiative energy and fuel consumption (Wooster et al. 2005). Both applications can inform fire management.

In addition, this study used a water balance approach to infer fuel moisture and productivity and to explore their potential to explain the spatial pattern of heat release from fire. Water demand and water loss were used to infer fuel moisture and fuel availability using established relationships which are linked to vegetation characteristics (photosynthesis capacity, root depth). Centered on different spatial and temporal contexts, the water balance approach was successful at a coarser scale than at the pixel level suggesting that the relationship between fire energy release and water balance variables was sensitive to the scale of analysis.

This study may serve as an example of what can limit expectations when dealing with remotely derived fire energy and surface-referred water budget variables at a microscale. First, data quality is crucial: calibration of the infrared imagery is required although it would not make a difference in pattern of heat release (calibration is linear). However, the detection limits at which the estimation of energy released can be reliable

appear to be a key point in order to properly classify heat release. Second, better site productivity measurements within the fire units and not in the vicinities are needed to validate growing season AET and to derive linear relationships as referred in the literature. These measurements can also be used to validate FRE.

Future work should couple the water balance model as applied in this study with a hydrological model in order to account for fine-scale soil moisture dynamics. During spring, ground flow regulates moisture patterns on the landscape (Matthew Dickinson, personal communication). Well-established methods exist to model hydrology of a site from elevation grids using cellular-automata, such as the TOPMODEL simulator of runoff of a catchment (Beyen and Kirkby 1979) or the GIS-based integrated moisture index (Iverson et al. 1997). The spatial analyst tool in the ArcGIS 9.3 has a hydrology toolbox that can be used to compute flow accumulation. Curvature or the shape of the surface can be also generated with this approach. Flow accumulation and curvature, both surface specific, account for gravitational movement of soil moisture that was not explicitly considered in this study. A multiple linear regression of fire energy release vs. PET and hydrology on one end, as well as fire energy release vs. AET and hydrology on the other end may fill in the gaps encountered in this study at the pixel level.

Another analysis that was not tried in this study is spatial autocorrelation or how correlated a variable is with itself through space. This spatial effect may contribute to the poor correlations at the pixel-level. Fire energy release, as seen in this study, tends to cluster in space. High values clustered with high values in their immediate vicinity, in particular on southern slopes; this is an example of positive spatial autocorrelation. Clusters of low-low values were also observed across the landscape, in particular on

northern slopes; this could also be an example of positive spatial autocorrelation. A negative spatial autocorrelation would cluster high values with low values in their proximity. Fotheringham et al. (2002) recommends a local measure of spatial autocorrelation when two cases of spatial autocorrelation (positive and negative) coexist within the same data set; thus, a local spatial autocorrelation would pick up these variations while a global approach would not. Moran's I is a good example for measuring local spatial autocorrelation; it can be computed with the spatial analyst in ArcGIS 9.3.

Spatial autocorrelation can be also applied to multivariate relationships, which are local versions of traditional regression analysis (i.e., spatially adaptive filtering, geographically weighted regression, etc.). This study did not consider this approach because variables of interest did not show relationships at the pixel level using a global random sampling. However, a multivariate spatial autocorrelation approach could be additionally used to explore locally the hypothesized relationships in this study. For example, clusters of high PET- high FRE or low PET- low FRE can inform about positive associations while clusters of high PET-low FRE or low PET-high FRE can suggest negative associations. Positive associations may confirm the hypothesis that PET controls fire energy release while negative correlations may contradict this hypothesis.

There is no fine-scale theory based on the hypothetical relationships of fire energy release vs. PET, and fire energy release vs. AET. Archibald et al. (2009) studied similar hypotheses at the continental scale using surrogate variables for fuel moisture and fuel availability, and fire variable different then this study. However, they found that fuel moisture and fuel load explained only 68% the variation of burnt area, for example. The theory is not well defined at the coarse-scale as well. Therefore, this study will continue

developing a fine-scale theory based on microscale drivers of fire energy release. Improved estimates of temperature, precipitation and soil moisture may improve the accuracy of the model. Better fuel measurements, ideally obtained simultaneously with AET and PET, will more accurately inform understanding of site productivity and fuel moisture, and will help to validate not only water balance variables but also remotely-retrieved fire energy.

REFERENCES

Albrecht MA, McCarthy BC (2006). Effects of prescribed fire and thinning on tree recruitment patterns in central hardwood forests. Forest Ecology and Management 226: 88-103.

Archibald S, Roy DP, Van Wilgen BW, Scholes RJ (2009). What limits fire? An examination of drivers of burnt area in Southern Africa. Global Change Biology 15: 613-630.

Bennie J, Huntley B, Wiltshire A, Hill MO, Baxter R (2008). Slope, aspect and climate: spatially explicit and implicit models of topographic microclimate in chalk grassland. Ecological Modeling 216: 47-59.

Beven KJ, Kirkby MJ (1979). A physically based, variable contributing area model of basin hydrology. Hydrological Sciences Bulletin 24: 43–69.

Braun EL (1950). Deciduous Forests of Eastern North America. Blakiston, Philadelphia

Budyko MI (1974). Climate and life, transl. from russian by Miller DH, Academic, San Diego, California.

Byram GM (1959). Combustion of forest fuels. In Forest Fire: Control and Use. McGraw-Hill, New York, pp 61-89.

Campbell GS (1977). An Introduction to Environmental Biophysics. Springer-Verlag, New York.

Campbell JB (1996). Introduction to Remote Sensing. Second edition, The Guilford Press, New York.

Davis KP (1959). Application of prescribed burning. In Forest fire: control and use. McGraw-Hill, New York, pp 507-537.

Dozier J (1981). A method for satellite identification of surface-temperature fields of subpixel resolution. Remote Sensing of Environment 11 (3): 221-229.

Dyer JM (2009). Assessing topographic patterns in moisture use and stress using a water balance approach. Landscape Ecology 24: 391-403.

Fotheringham AS, Brunsdon C, Charlton M (2002). Geographically weighted regression. The analysis of spatially varying relationships. John Willey & Sons, England.

Freeborn PH, Wooster MJ, Hao WM, Ryan CA, Nordgren BL, Baker SP, Ichoku C (2008). Relationships between energy release, fuel mass loss, and trace gas and aerosol emissions during laboratory biomass fires. Journal of Geophysical Research-Atmospheres 113: 1-17.

Gerrits AMJ, Savanije HHG, Veling EJM, Pfister L (2009). Analytical derivation of the Budyko curve based on rainfall characteristics and a simple evaporation model. Water Resour. Res. 45, W04403, doi:10.1029/2008WR007308.

Giglio L, Kendall JD (2001). Application of the Dozier retrieval to wildfire characterization - A sensitivity analysis. Remote Sensing of Environment 77 (1): 31-49.

Girardin MP, Wotton BM (2009). Summer moisture and wildfire risks across Canada. Journal of Applied Meteorology and Climatology 48: 517-533.

Hirsch SN, Kruckerberg RF, Madden FH (1971). The bi-spectral forest fire detection system. Proceedings of the 7th international symposium on remote sensing

environment, 17-21 May 1971: 2253-2272. Ann Arbor: Environmental Research Institute of Michigan.

Hutchinson TF, Sutherland EK, Yaussy DA (2005). Effects of repeated prescribed fires on the structure, composition, and regeneration of mixed-oak forests in Ohio. Forest Ecology and Management 218: 210-228.

Ichoku C, Martins JV, Kaufman YJ, Wooster MJ, Freeborn PH, Hao WM, Baker S, Ryan CA, Nordgren BL (2008). Laboratory investigation of fire radiative energy and smoke aerosol emissions. Journal of Geophysical Research-Atmospheres 113: 1-11.

Iverson LR, Dale ME, Scott CT, Prasad A (1997). A GIS-derived integrated moisture index to predict forest composition and productivity of Ohio forests (U.S.A.). Landscape Ecology 12: 331-348.

Johnson EA, Miyanishi K (2001). Forest Fires Behavior and ecological Effects. Academic Press, San Diego, CA.

Justice CO, Giglio L, Korontzi S, Owens J, Morisette JT, Descloiters J, Alleaume S, Petitcolin F, Kaufman Y (2002). The MODIS fire products. Remote Sensing of Environment 83 (1-2): 244-262.

Kaufman Y, Remer L, Ottmar R, Ward D, Rong L, Kleidman R, Fraser R, Flynn L, McDougal D, Shelton G (1996). Relationship between remotely sensed fire intensity and rate of emission of smoke: SCAR-C experiment. In J. Levine (Ed.), Global biomass burning: MIT Press, Massachusetts, pp 685-696.

Kaufman Y, Justice CO, Flynn LP, Kendall JD, Prins EM, Giglio L, Ward DE, Menzel WP, Setzer AW (1998). Potential global fire monitoring from EOS-MODIS. Journal of Geophysical Research 103: 32215-32238.

Kaufman Y, Kleidman RG, King MD (1998). SCAR-B fires in the tropics: properties and remote sensing from EOS-MODIS. Journal of Geophysical Research 103: 31955-31968.

Mather JR (1974). Climatology: fundamentals and applications. McGraw-Hill, New York.

McVicar TR, Van Niel TG, LT Li, Hutchinson MF, Mu XM, Liu ZH (2007). Spatially distributing monthly reference evapotranspiration and pan evaporation considering topographic influences. Journal of Hydrology 338: 196-220.

National Oceanic and Atmospheric Administration (NOAA) (2009). National Climatic Center, Climvis Information. http://www.ncdc.noaa.gov/onlinrprod

Natural Resources Conservation Service, Soil Survey Staff (2008) Soil Survey Geographic (SSURGO) Database. United States Department of Agriculture. URL: http:// soildatamart.nrcs.usda.gov

Nepstad D, Lefebvre P, Da Silva UL, Tomasella J, Schlesinger P, Slorzano L, Moutinho P, Ray D, Benita JG (2004). Amazon drought and its implications for forest flammability and tree growth: a basin-wide analysis. Global Change Biology 10: 704-717.

Oertel D, Briess K, Halle W, Neidhardt M, Lorenz E, Sandau R, Schrandt F, Skrbek W, Venus H, Walter I, Zender B, Zhukov B, Goldammer JG, Held AC, Hille M,

Brueggemann H (2003). Airborne forest fire mapping with an adaptive infrared sensor. International Journal of Remote Sensing 24 (18): 3663-3682.

Ohio Geographically Referenced Information Program (2008) Ohio Statewide Imagery Program. URL: http://ogrip.oit.ohio.gov/ServicesData/StatewideImagery/tabid/86/Default.aspx

Ononye AE, Vodacek A, Li Y, Wang Z (2005). Mapping of active fire area by image gradient techniques. Forest Service Remote Sensing Applications Conference, Salt Lake City, Utah, April 5-9.

Ononye AE, Vodacek A, Saber E (2007). Automated extraction of fire line parameters from multispectral infrared images. Remote Sensing of Environment 108: 179-188.

Parker JR (1997). Algorithms for image processing and computer vision. John Wiley & Sons, Inc., New York.

Porporato A, Daly E, Rodrguez-Iturbe I (2004). Soil water balance and ecosystem response to climate change. American Naturalist 164(5): 625-632.

Potter NJ, Zhang L, Milly PCD, McMahon TA, Jakeman AJ (2005). Effects of rainfall seasonality and soil moisture capacity on mean annual water balance for Australian catchments. Water Resources Research 41,W06007, doi:10.1029/2004WR003697.

Prins EM, Feltz JM, Menzel WP, Ward DE (1998). An overview of GOES-8 diurnal fire and smoke results for SCAR-B and 1995 fire season in South America. Journal of Geophysical Research-Atmospheres 103 (D24): 31821-31835.

PRISM Climate group, Oregon State University (2008). URL: http://www.prismclimate.org, created 4 Feb 2004.

Riggan PJ, Tissell RG, Lockwood RN, Brass JA, Pereira JAR, Miranda HS, Miranda AC, Campos T, Higgins R (2004). Remote measurement of energy and carbon flux from wildfires in Brazil. Ecological Applications 14 (3): 855-872.

Roberts GJ, Wooster MJ (2008). Fire detection and fire characterization over Africa using Meteosat SEVIRI. IEEE transactions on geosciences and remote sensing 46 (4): 1200-1218.

Robinson JM (1991). Fire from space – global fire evaluation using infrared remote-sensing. International Journal of Remote Sensing 12 (1): 3-24.

Rosenzweig ML (1968). Net primary productivity of terrestrial communities: prediction from climatological data. The American Naturalist 102 (923): 67-74.

Rothermel RC (1972). A mathematical model for predicting fire spread in wildland fuels. USDA Forest Service, Research Paper INT-115.

Scalia Laboratory, Department of Geography, Ohio University (2008). URL: http://www.scalialab.com/

Scholes RJ, Kendall J, Justice CO (1996). The quantity of biomass burned in southern Africa. Journal of Geophysical Research-Atmospheres 101 (D19): 23667-23676.

Slocum TA, McMaster RB, Kressler FG, Horward HG (2005). Thematic Cartography and Geographic Visualization, Pearson Prentice Hall, NJ.

Smith AMS, Wooster MJ (2005). Remote classification of head and backfire types from MODIS fire radiative power and smoke plume observations. International Journal of Wildland Fire 14 (3): 249-254.

Trollope WSW, Trollope LA, Potgieter AFL, Zambatis N (1996). SAFARI-92 characterization of biomass and fire behavior in the small experimental burns in the Kruger National Park. Journal of Geophysical Research-Atmospheres 101 (D19): 23531-23539.

Turc L (1961) Evaluation des besoins en eau d'irrigation, évapotranspiration potentielle, formule climatique simplifiée et mise à jour. *Ann Agron* 12:13-49.

Waggoner J (1991). Airborne system locates fires. Photonics Spectra 25, 22.

Viegas DX (2002). Fire line rotation as a mechanism for fire spread on a uniform slope. International Journal of Wildland Fire 11: 11-23.

Wendt CK, Beringer J, Tapper NJ, Hutley LB (2007). Local boundary-layer development over burnt and unburnt tropical savanna: an observational study. Boundary-Layer Meteorology 124: 291-304.

Wooster MJ (2002). Small-scale experimental testing of fire radiative energy for quantifying mass combusted in natural vegetation fires. Geophysical Research Letters 29: Art. No. 2027.

Wooster MJ, Zhukov B, Oertel D (2003). Fire radiative energy for quantitative study of biomass burning: derivation from the BIRD experimental satellite and comparison to MODIS fire products. Remote Sensing of Environment 86: 83-107.

Wooster MJ, Roberts G, Perry GLW, YJ Kaufman (2005). Retrieval of biomass combustion rates and totals from fire radiative power observations: FRP derivation and calibration relationships between biomass consumption and fire radiative energy release. Journal of Geophysical Research-Atmospheres 110 (D24): Art. No. D24311.

Yang D, Shao W, Yeh PJ-F, Yang H, Kanae S (2009). Impact of vegetation coverage on regional water balance in the nonhumid regions of China. Water Resources Research 45, W00A14, doi:10.1029/2008WR006948.

Zhang L, Potter N, Hickel K, Zhang Y, Shao Q (2008). Water balance modeling over variable time scales based on the Budyko framework - Model development and testing. Journal of Hydrology, 360: 117-131.